



Enhanced removal of basic dye using carbon nitride/graphene oxide nanocomposites as adsorbents: high performance, recycling, and mechanism

Junia Teixeira Martins¹ · Carlos Henrique Guimarães¹ · Paula Mayara Silva¹ · Rafael L. Oliveira² · Patricia Prediger¹ 

Received: 19 June 2020 / Accepted: 8 September 2020 / Published online: 11 September 2020
© Springer-Verlag GmbH Germany, part of Springer Nature 2020

Abstract

The presence of dyes in wastewater streams poses a great challenge for sustainability and brings the need to develop technologies to treat effluent streams. Here, we propose a mixture of high superficial area carbon-based nanomaterial strategy to improve the removal of basic blue 26 (BB26) by blending porous carbon nitride (CN) and graphene oxide (GO). We prepared CN and GO pristine materials, as well the nanocomposites with mass/ratio 30/70, 50/50, and 70/30, and applied them into BB26 uptake. Nanocomposite 50/50 CN/GO was found to be the better adsorbent, and the optimization of the adsorption revealed a fast equilibrium time of 30 min, after sonication for 2 min, nanocomposite 50/50, and BB26 dye loading of 0.1 g/L and 100 mg/L, respectively. The pH variation had great influence on BB26 uptake, and at ultrapure water pH, the dye removal capacity by the composite reached 917.78 mg/g. At pH 2, a remarkable removal efficiency of 3510.10 mg/g was obtained, probably due to electrostatic interactions among protonated amine groups of the dye and negatively charged CN/GO nanocomposite. The results obtained were best fitted to the pseudo-second-order kinetic model and the Dubinin–Radushkevich isotherm. The adsorption process was thermodynamically spontaneous, and physisorption was the main mechanism, which is based on weak electrostatic and π – π interactions. The dye attached to the CN/GO nanocomposite could be removed by washing with ethyl alcohol, and the adsorbent was reused for five consecutive cycles with high BB26 uptake efficiency. The CN/GO nanocomposite ability to remove the BB26 dye was 21 times higher than those reported in the literature, indicating CN/GO composites as potential filtering materials to basic dyes.

Keywords Graphene oxide Porous carbon nitride Adsorption Basic dye Water purification

Highlights

- CN/GO nanocomposites are better adsorbents to BB26 dye than pristine materials.
- Electrostatic interactions are the main mechanism in BB26 removal by CN/GO composite.
- Very fast kinetics in BB26 adsorption.
- High BB26 removal capacities (917 mg/g at pH 6 and 3510 mg/g at pH 2).
- Successful CN/GO nanocomposite recycling.

Responsible Editor: Tito Roberto Cadaval Jr

Electronic supplementary material The online version of this article (<https://doi.org/10.1007/s11356-020-10779-z>) contains supplementary material, which is available to authorized users.

✉ Patricia Prediger
prediger@unicamp.br

¹ School of Technology, University of Campinas – Unicamp, Limeira, CEP, São Paulo 13484-332, Brazil

² Fakultät II, Institut für Chemie: Funktionsmaterialien, Sekretariat BA2, Technische Universität Berlin, Hardenbergstraße 40, 10623 Berlin, Germany

Introduction

Synthetic cationic dyes based on triphenylmethane are widely used in various industries such as tanning, paper and cellulose, ink, textiles, food, cosmetics, and pharmaceuticals. The wastewater of these industrial processes has a high load of this class of dyes (Gupta and Suhas 2009; Chen et al. 2016), which currently gain prominence as an environmental pollutant for being considered toxic to aquatic life (Chen et al. 2010; Ding et al. 2012; Belpaire et al. 2015). In addition, dyes absorb and reflect sunlight, interfering directly in bacterial growth and the photosynthesis process of aquatic plants, resulting in a lower rate of water oxygenation and limiting biological degradation of impurities in water (Allen et al. 2004).

Basic blue 26 (BB26—Fig. 1) belongs to the class of cationic triphenylmethane dyes. These compounds are characterized by the presence of the chromogen group that has phenyl groups bound by the central carbon atom (Przystas et al.

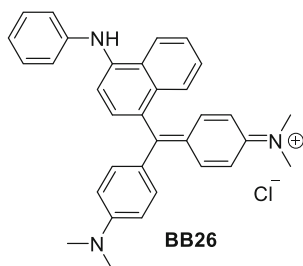


Fig. 1 Chemical structure of the basic blue 26 dye

2012), being thus a complex molecular structure of hard degradation (Rai et al. 2005). Several studies have been dedicated to the removal of triphenylmethane dyes in wastewater through adsorption (Pei et al. 2016), flocculation (Penner and Lagaly 2000), photocatalysis (Roushani et al. 2015), and biodegradation (Chen et al. 2016). Adsorption studies for BB26 removal were described using several materials (Khare et al. 1987; Kumar et al. 2013; Anirudhan et al. 2014; Kataria et al. 2016; de Souza et al. 2018, 2019) in which the best result was achieved with zinc oxide nanoparticles and 163 mg/g of removal capacity (Kataria et al. 2016). However, all these studies had drawbacks such as long removal times and low rates of reuse.

The materials used for adsorption have specific characteristics, such as high surface area and chemical stability (Lee et al. 2015; Xu et al. 2016; Zhao et al. 2016). Carbon nitride (CN)– and graphene oxide (GO)–based composites are viable options for this purpose. GO can be obtained by oxidizing natural graphite, an abundant and inexpensive material; graphene derivatives in general have high adsorption capacity and fast equilibrium rates associated with a wide range of pH and temperature, which is responsible for nanostructure and high energy conductivity (Prediger et al. 2018). CN can be obtained by thermal treatment of urea or cyanamide under inert atmosphere, and this treatment leads to the formation of a low surface area CN—for this reason, a hard-template methodology is used to increase the surface area of carbon nitride and to introduce pores (Zhang et al. 2013; Oliveira et al. 2020). This material has high physical and chemical stability and low toxicity (Xu et al. 2019). It also has an excellent response to visible light and has been used as a catalytic material for several processes. In the literature, few examples of mesoporous CN have been applied for adsorption of pollutants in water, and its usage for pollutant adsorption is still incipient (Shi et al. 2020; Tian et al. 2020; Yi et al. 2020).

To enhance some properties such as surface area, porosity, photocatalytic activity, dispersion, and specific anchoring sites, nanocomposites based on CN/GO have been prepared and applied to detect pesticides (Xiao et al. 2020) and drugs (Hu et al. 2018), and degradation of organic pollutants (Joseph et al. 2019). There are few reports in the literature that describe the use of CN/GO composites in pollutant adsorption from water, and usually, adsorption is accompanied by

photocatalytic degradation (Xu et al. 2019). Recently, Li et al. described the preparation of *S*-doped CN/GO nanocomposites and its evaluation as adsorbent of mercury ions (Li et al. 2020). The CN/GO composite characterization revealed a porous three-dimensional adsorbent that showed high Hg^{2+} removal and low toxicity, suggesting CN/GO composites as a potential candidate for environmental applications.

In this study, porous CN and GO were synthesized and further combined to generate new nanocomposites (CN/GO mass ratio 30/70, 50/50, 70/30) that had the best characteristics of each material, resulting in a material with greater efficiency for the removal of basic dye in water. Thus, the generated materials were characterized and applied to BB26 removal. The sorption process was assessed by varying the proportions of pristine materials in the nanocomposites, as well as the variation of pH, temperature, contact time, sonication irradiation, and adsorbent/dye concentration. We also analyzed adsorption kinetics, isotherms, thermodynamic parameters, and recycling to study the adsorption characteristics and mechanisms of interactions between BB26 dye and porous CN/GO nanocomposites. To the best of our knowledge, it is the first time that a dye adsorption process has been studied and optimized using CN/GO nanocomposites as adsorbents.

Materials and methods

Chemical reagents

The natural graphite powder was obtained from Nacional de Grafite LTDA (code: Micrograf 99507 UJ). Potassium permanganate (KMnO_4), potassium sulfate (K_2SO_4), and sodium nitrate (NaNO_3) were purchased from Acros Organics (Geel, Belgium); concentrated sulfuric acid (H_2SO_4 , 98%), hydrochloric acid (HCl, 37%), and ethanol ($\text{C}_2\text{H}_5\text{OH}$, 99.5%) were purchased from Labsynth (Diadema, SP, Brazil); hydrogen peroxide (H_2O_2 , 30%), HS-40 solution (40 wt% in H_2O), cyanamide (99%), and phosphorus pentoxide (P_2O_5) were purchased from Sigma-Aldrich (Milwaukee, WI, USA). Ammonium-bifluoride (97%) was obtained from VWR Chemicals. BB26 dye was acquired by Danny Color Corantes (São Paulo, SP, Brazil).

Graphene oxide synthesis

GO was synthesized by successive chemical reactions, starting with graphite pre-oxidation (de Figueiredo Neves et al. 2020b, a). Thus, 20 g of graphite was oxidized using 120 mL of concentrated H_2SO_4 , 10 g of K_2SO_4 , and 10 g of P_2O_5 for 6 h at 353 K. The crude product was slowly added in ultrapure water (1 L) under an ice bath. Subsequently, the crude product was submitted to vacuum filtration and washed with ultrapure water until pH 6.

Then, the pre-oxidized graphite was dried and the GO synthesis followed the modified Hummers protocol (Hummers and Offeman 1958). Into an Erlenmeyer flask, under magnetic stirring and ice bath, pre-oxidized graphite and 500 mL of concentrated H_2SO_4 were added. Then, 10 g of sodium nitrate (NaNO_3) was slowly added to the reaction mixture, as well as 60 g of potassium permanganate (KMnO_4). The reaction was controlled so the temperature did not exceed 313 K. Afterwards, the reaction mixture was maintained under magnetic stirring and ice bath for 1 h, and after that, the stirring was then maintained for 7 days at room temperature. Thus, the reaction was cooled by using an ice bath and ultrapure water was slowly added (2 L). Then, 100 mL of hydrogen peroxide aqueous solution (H_2O_2 , 3% v/v) was added drop by drop. The crude product was heated at 373 K for 30 min. Immediately after heating, the crude product was submitted to vacuum filtration and washed with a solution containing 3% sulfuric acid and 0.5% hydrogen peroxide (10 L). Continuing the washing step, a 10% HCl aqueous solution (20 L) was used followed by ultrapure water until pH 5 was reached.

Porous CN synthesis

For the synthesis of this porous carbon nitride, silica nanoparticles (HS-40) were used as a template. One gram of cyanamide was dissolved in methanol (7.0 mL); subsequently, this solution was added into a 100-mL round-bottom flask containing 1 g of silica. The solvents were removed by the use of

rotatory evaporator, and the obtained powder was then calcinated for 6 h at 823 K under an argon atmosphere. A solution of ammonium-bifluoride (50 mL, 4 M) was then added to the obtained light-yellow powder, and the system was stirred for 24 h. After the silica removal, the solid was filtered and washed with water (500 mL) and ethanol (1×100 mL). The solid was then dried at 353 K for 24 h.

Preparation of GO- and CN-based nanocomposites

The CN/GO nanocomposites were prepared by varying the loading of the constituents (mass ratio 30/70, 50/50, and 70/30). In this regard, GO dispersed in water and previously stirred for 30 min at room temperature was used. The appropriate amount of CN also dispersed in water at room temperature was sonicated for 10 min. Subsequently, CN suspension was added to the GO and it was sonicated for 30 min. The suspension obtained was stored in a refrigerator to be used later. In Fig. 2, it is presented the protocol for obtaining the nanocomposites based on GO and CN.

Characterization

The materials were characterized by using atomic force microscopy (AFM), through the Analysis NanoIR2-s equipment, using 512×512 resolution and image treatment with the Gwyddion software. To the pristine materials, it was extracted a profile to calculate the thickness and width. Infrared spectroscopy with Fourier transformation (FTIR) was made by

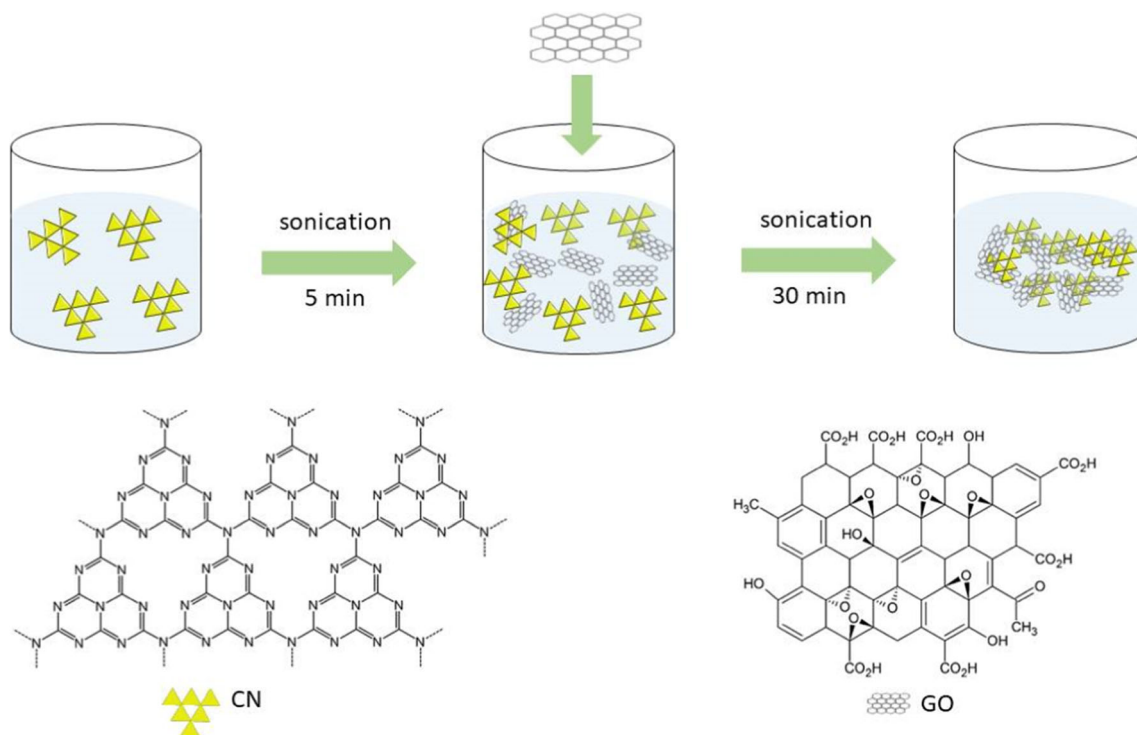


Fig. 2 CN/GO nanocomposite preparation

using a FTIR Agilent - Cary 360 equipment, in a range of 400 to 4000 cm^{-1} , and the KBr method. Raman spectroscopy was performed through a confocal Horiba Jobin Yvon T6400 equipment with a CCD detector and Olympus BX41 microscopy, in a range of 200 to 3300 cm^{-1} , resolution of 1 cm^{-1} ; $n^\circ 1$ filter; and laser at 532 nm with a potency of 1 mW. The materials were analyzed through X-ray diffraction (XRD) through Panalytical model X'Pert Powder XRD, in a range of 5 to 100° and operation at 40 kV and 30 mA. The morphology and sizes of GO and CN were determined with LEO electron microscopy model Leo 440i. Scanning electron microscopy (SEM) samples were prepared by placing a suspension drop onto a silicon wafer and being dried under high vacuum. The Brunauer–Emmett–Teller (BET) surface area of GO, CN, and nanocomposites was assessed via nitrogen adsorption experiments. Nitrogen physisorption measurements were performed at 77 K using a Quantachrome model NOVA 4200e. The samples were dried before measurement under vacuum at 140 °C for at least 12 h. Transmission electron microscopy (TEM) images were obtained from a FEI Tecnai G2 20 STWIN microscope at an operating voltage of 200 kV.

Adsorption experiments

The adsorption experiments were performed in triplicate using up to 0.75 mL of the material suspension. The adsorbent was sonicated before each adsorption experiment, except for the sonication time optimization. The BB26 dye solution (up to 4.25 mL) was added to the beaker, and the mixture was stirred at 150 rpm on a thermo-regulated oscillatory shaker for 30 min, and the aliquots were removed to study the adsorption effect. Subsequently, the collected aliquots were centrifuged and the supernatant was analyzed using a GBC Cintra 6 spectrophotometer at a maximum absorbance of 620 nm.

The parameters that affect the adsorption process were investigated: pH (2–10), temperature (298–328 K), sonication time (0–90 min), nanomaterial concentration (0.05–0.4 g/L), and time (0.5–480 min). All the experiments were carried out in ultrapure water natural pH; when necessary, pH adjustments were performed with the addition of HCl and NaOH solutions. The adsorption capacity of the BB26 onto pristine GO or CN and CN/GO nanocomposites and the removal efficiency were calculated using Eq. 1 and Eq. 2 (Al-Zboon 2018):

$$q_e = (C_o - C_e) \cdot \frac{V}{m} \tag{1}$$

$$\text{Removal efficiency (\%)} = \frac{(C_o - C_e)}{C_o} \cdot 100 \tag{2}$$

q_e is the amount of dye adsorbed onto by the amount of the adsorbent (mg/g), C_o and C_e are the BB26 dye concentrations

before and after the experiment (mg/L), V is the total volume of the experiment (L), and m is the mass of the adsorbent (g).

The recycling experiments were performed as follows: the first adsorption cycle was performed with 20 mL of CN/GO (0.2 g/L) and BB26 (180 mL, 100 mg/L). The adsorption tests were performed at pH 2 at room temperature. The CN/GO loaded with BB26 was recovered after each adsorption process. The nanocomposite/BB26 loaded was centrifuged at 3500 rpm for 15 min, and the supernatant was removed using micropipettes.

The recovered CN/GO was first carefully washed with ultrapure water, centrifuged, and the aqueous phase removed in a rotatory evaporator. The obtained solid was then washed with ethanol, centrifuged, and the aqueous phase removed with micropipette. The washing with ethanol was performed twice. The solid obtained was dried at 318 K and then used in the adsorption process. The recycling and desorption experiments were performed in triplicate.

The kinetic and isothermal parameters were determined by using the add-in Solver from Microsoft sheets.

Results and discussions

CN/GO composite characterization

Brunauer–Emmett–Teller

The N_2 physisorption analyses at 77 K were performed to get information about the specific surface area of CN, GO, and related nanocomposites. The data obtained for the BET specific surface area of CN was 200.3 m^2/g , and the pore volume was 0.88 cm^3/g , being these values in the same magnitude of porous carbon nitride previously reported (Wang et al. 2018; Burrow et al. 2020). Pristine GO had a superficial area of 213.0 m^2/g , which is similar to those previously reported (Prediger et al. 2018). The BET surface area for 30/70, 50/50, and 70/30 CN/GO nanocomposites were 96.9, 89.7, 110.6 m^2/g , respectively. Considering that the validity of the simplifying assumption is frequently within the variation of surface area measurements— $\pm 10\%$ for different materials (Sing et al. 1985)—the nanocomposites showed similar results and no relevant difference between the measured surface areas. The obtained surface area for CN/GO nanocomposites was similar to those reported by Svoboda et al. (2019) to CN/GO (mass/ratio 20/80, 33/67, 50/50, and 75/25). The BET surface area obtained from GO and composites is much lower than the theoretical values for isolated particles and graphene sheets. This might be due to overlapping and coalescing of these materials during the drying process.

Fourier-transform infrared spectroscopy

Chemical groups in the pristine materials and nanocomposites were analyzed by using FTIR, and the obtained spectra are shown in Fig. 3. CN spectrum shows bands at 807 cm^{-1} , which belongs to the tri-*s*-triazine groups (triazine ring) and is the most characteristic CN peak. The bands at 1255 cm^{-1} , 1324 cm^{-1} , 1424 cm^{-1} , 1575 cm^{-1} , and 1631 cm^{-1} indicate the presence of aromatic heterocycles. The band at 2175 cm^{-1} confirms the presence of residual cyanide groups (Desipio et al. 2019), and the bands at 3181 cm^{-1} and 3342 cm^{-1} are due to NH and OH bond stretching (N–H, O–H) (Wan et al. 2019). In relation to the GO spectrum, we noted bands at 1076 cm^{-1} and 1387 cm^{-1} , which refer to C–O and C–OH stretching bonds. The bands at 1628 cm^{-1} and 1728 cm^{-1} are assigned to C=C and C=O stretching vibration bonds, respectively, while those at 3441 cm^{-1} are associated with hydrogen bonds (O–H) (Gao et al. 2016; Luo et al. 2019). In the nanocomposite spectra, the band at 1728 cm^{-1} (C=O) and 1076 cm^{-1} (C–O) that referred to the GO spectrum and bands at 2175 cm^{-1} (residual cyanide groups) and 1575 cm^{-1} (aromatic heterocycles) that referred to the CN spectrum are absent. We can find peaks at 1631 cm^{-1} , 1425 cm^{-1} , 1321 cm^{-1} , 1255 cm^{-1} , and 807 cm^{-1} . These indicate that the composites carry characteristics of both pristine materials.

Raman spectroscopy

Material structure and disorders in the graphene structure formed by sp^2 -hybridized carbon atoms arranged in a crystalline honeycomb lattice were analyzed through Raman spectroscopy, and the spectra of GO and nanocomposite CN/GO (30/70, 50/50, 70/30) are shown in Fig. 4. In all the spectra, it was verified the bands at 1348 cm^{-1} and 1590 cm^{-1} , which are associated with the D and G bands, respectively. The D band indicates the defects in the carbon plan, and the G band refers to the carbon stretching (Zhang et al. 2014b). With the D and

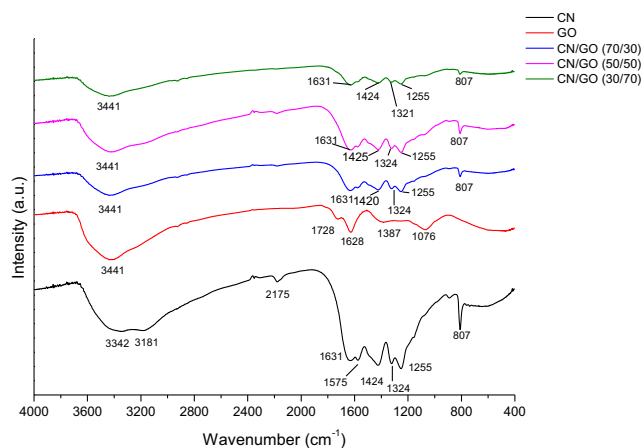


Fig. 3 FTIR spectra. CN, GO, and nanocomposite CN/GO (30/70, 50/50, and 70/30), in a range of 400 to 4000 cm^{-1}

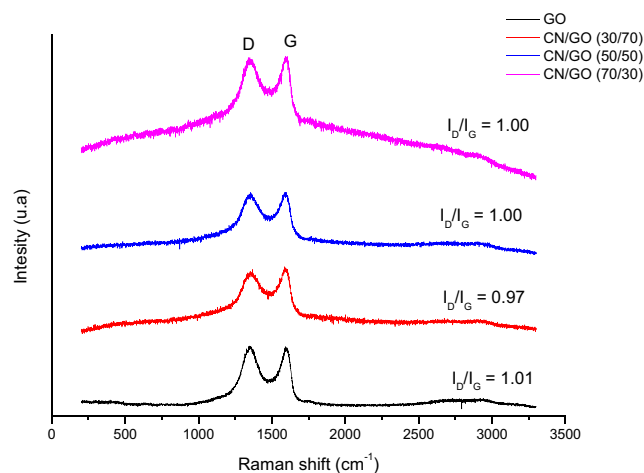


Fig. 4 Raman spectra. CN, GO, and nanocomposite CN/GO (30/70, 50/50, 70/70), in a range of 200 to 3300 cm^{-1}

G band intensity, we calculated the I_D/I_G index for each material. All the I_D/I_G ratios obtained were similar, indicating that the generation of the CN/GO nanocomposites had not changed its structure or caused an increment in disorder. Pristine CN could not be analyzed because of its fluorescence under the applied conditions (Hernández-Torres et al. 2016).

X-ray diffraction

Material structure and its crystallography were analyzed by XRD, whose patterns were used for phase identification of the crystalline material. The obtained XRD patterns of CN, GO, and nanocomposite CN/GO (30/70, 50/50, and 70/30) are shown in Fig. 5. Concerning the CN pattern, we highlighted two peaks at 12.2° (100) and 27.5° (002), which indicate the presence of an in-plane tri-*s*-triazine framework parallel to the *c*-axis and periodic graphitic layers along the *c*-axis, respectively (Chen et al. 2015; Gao et al. 2016). The GO pattern shows a peak at 10.7° (002), which was applied in Bragg's law to calculate the interlayer distance. This distance was 0.82

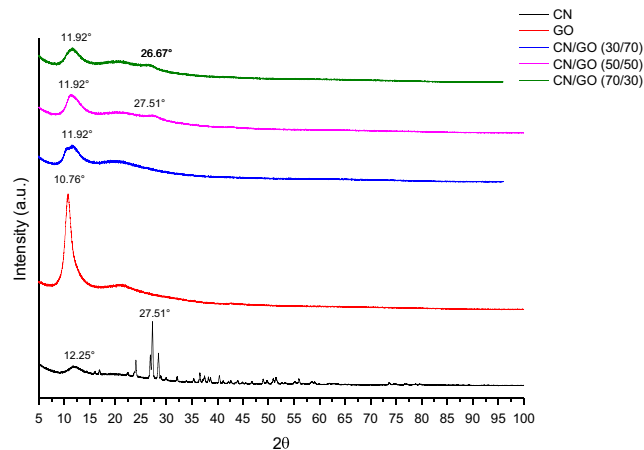


Fig. 5 XRD patterns. CN, GO, and nanocomposite CN/GO (30/70, 50/50, 70/30), in a range of 5 to 100°

nm, which is similar to the value observed by Zhang et al. (2014b). Regarding nanocomposite’s patterns, we observed peaks at 11.92°, a value near the peak verified in the precursor’s pattern, GO (10.7°) and porous CN (12.2°). The 11.92° peak is sharper than those seen in the CN pattern; however, it is less intense than that verified in GO. In the XRD pattern of the CN/GO composites 70/30 and 50/50, which have superior CN content, we found peaks at 27.5° and 26.6°, respectively. These peaks correspond to the crystallographic plan 002 of the pristine CN material. When compared with the CN pattern, these peaks are wider and less intense (Guo et al. 2016).

Scanning electron microscopy

We analyzed the morphology of pristine CN and GO and nanocomposites with SEM microscopic tools, and the obtained images are presented in Fig. 6. The SEM image of GO (Fig. 6a) shows an agglomerate of packed lamellar structures indicating the multilayered nanosheets. The CN image (Fig. 6b) reveals that CN has a non-specific morphology with a broad particle size distribution. Figure 6c–e refer to the SEM images of the CN/GO nanocomposites (30/70, 50/50, 70/30). Both pristine materials could be verified in the composite images,

and, in most cases, we could observe the GO nanosheets interacting with the CN porous structures.

Atomic force microscopy and transmission electron microscopy

TEM images of pristine CN and GO are shown in Fig. 7. These images (Fig. 7b and c) present a porous structure of the synthesized carbon nitride, where the pores have the same range of size of the silica particles, suggesting the formation of a 3D porous structure as shown in the scheme (Fig. 7a). Figure 7d shows a typical image of a GO nanosheet.

Pristine GO and nanocomposite material morphology were analyzed through AFM (Fig. 8). Pristine GO (Fig. 8a) is shown as monolayer nanosheets, and the AFM profile (Fig. 8b) indicates a width of 1.41 μm and thickness of 0.87 nm, as it is expected for this material and reported in the literature (Hummers and Offeman 1958; Eftekhari and Fan 2017). Concerning the CN/GO nanocomposites, the AFM image (Fig. 8c–e) revealed the presence of both pristine materials. Some CN particles (bright round particles) are attached to GO, indicating the presence of interactions between the materials. Figure 8f shows the images of diluted aqueous suspensions of

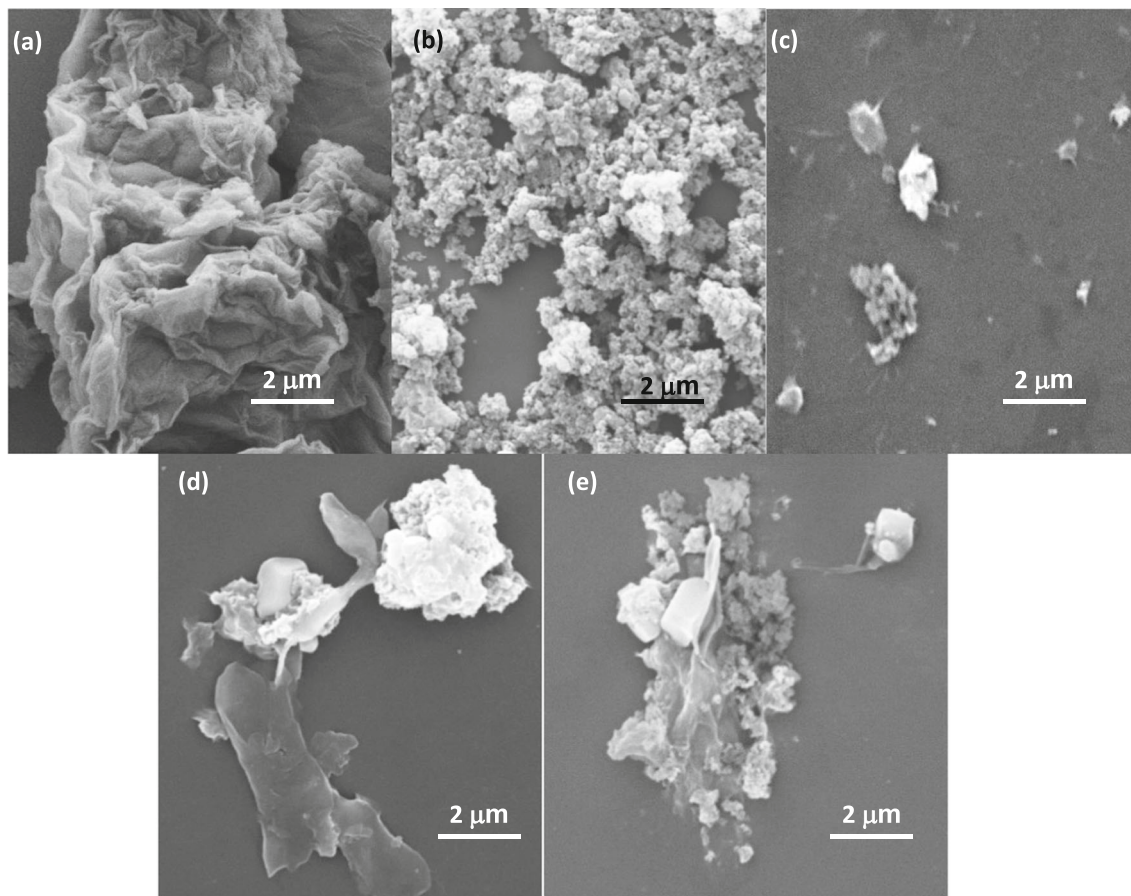


Fig. 6 SEM microcopies of **a** pristine GO; **b** pristine CN; and CN/GO nanocomposites **c** 30/70, **d** 50/50, **e** 70/30

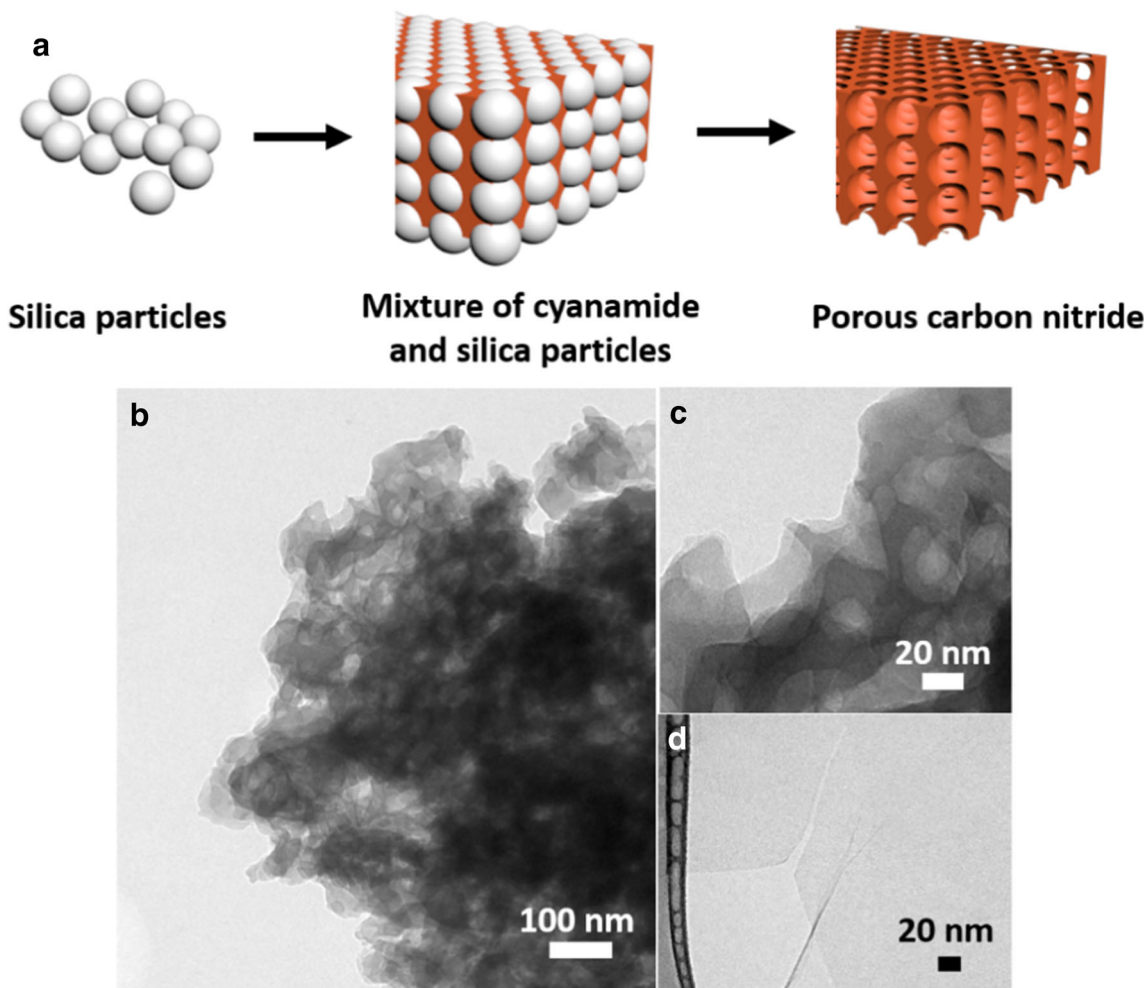


Fig. 7 a Scheme of mesoporous carbon nitride preparation. b, c TEM images of porous CN. d TEM image of GO

composites CN/GO 30/70, 50/50, and 70/30, indicating that the higher the CN content, the more opaque the suspension is.

Optimization of the BB26 dye adsorption process

Effect of the BB26 dye concentration and the proportion variance of the materials

At the beginning of the optimization, all the three nanocomposites and pristine materials were evaluated as potential adsorbents of the basic dye removal from water. For this purpose, the experiments were carried out with BB26 at the concentration of 200 mg/L and 0.05 g/L of adsorbent dose. The contact time of the adsorption process was 30 min.

Figure 9 shows that when pristine CN and GO were used as adsorbent, lower removal efficiencies were reached: 251 mg/g (63%) and 366 mg/g (91%), respectively. When the nanocomposites containing higher GO loading (CN/GO 30/70 and 50/50) were used, the maximum percentage removal (99%) and a superior removal capacity were observed, 398 and 390 mg/g, respectively. The nanocomposite 70/30 had lower

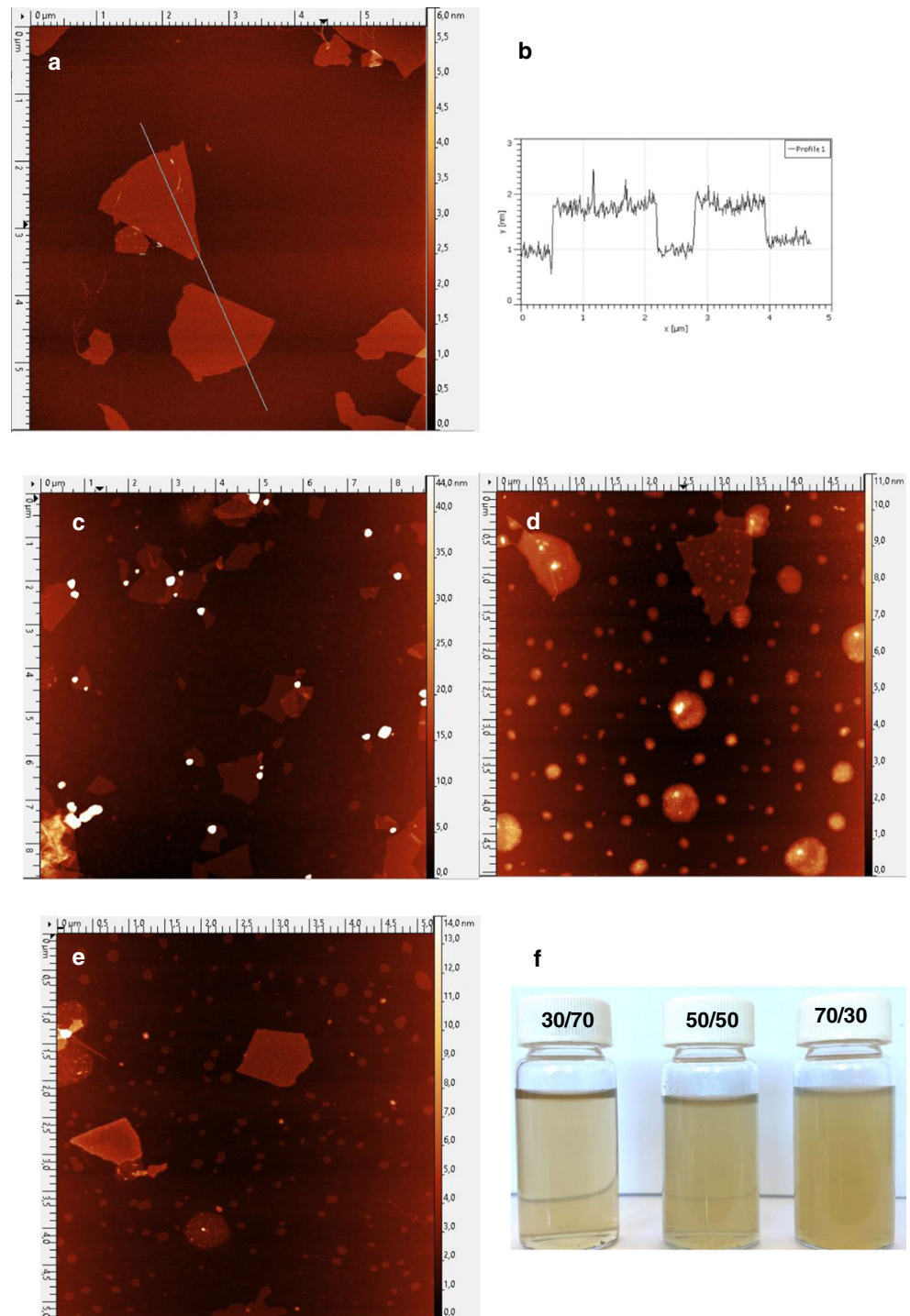
performance (370 mg/g—91%). These results are probably due to the improvement in the adsorbent structure caused by the presence of highly porous CN and flat GO nanosheets. The 3D CN adsorbent provides a fair possibility for BB26 dye to be adsorbed. The combination of the two materials provided the dye to interact with the adsorbent by electrostatic and π - π interactions.

Overall, CN/GO nanocomposites had better results than pristine materials. The nanocomposite chosen for the optimization process was the 50/50 CN/GO, since this adsorbent furnished an excellent BB26 dye uptake and it is formed by equal proportion of the pristine materials. The q_e obtained and the percentage removal of the BB26 dye are great results when compared with other sorbent materials (Anirudhan et al. 2014; Liu et al. 2019), suggesting that these nanocomposites are potential filtering agents of basic dyes.

Effect of contact time

The contact time is a crucial factor for dye removal due to the physical and chemical interactions between

Fig. 8 **a** AFM images of pristine GO with a resolution of $5\ \mu\text{m} \times 5\ \mu\text{m}$. **b** The height profile of the AFM image. **c** CN/GO (30/70) image with a resolution of $8\ \mu\text{m} \times 8\ \mu\text{m}$. **d** CN/GO (50/50) and **e** CN/GO (70/30) both with resolution of $5\ \mu\text{m} \times 5\ \mu\text{m}$. **f** Images of diluted aqueous suspensions of the nanocomposites CN/GO 30/70, 50/50, and 70/30



sorbent and sorbate. BB26 sorption experiments onto CN/GO (50/50) nanocomposite were carried out in triplicate in the range from 0 to 480 min (Fig. 10). The BB26 dye concentration was reduced to 100 mg/L with the purpose of optimizing the contact time, since the tests with 200 mg/L achieved the maximum in efficiency.

The BB26 uptake efficiency by the nanocomposite CN/GO 50/50 was measured in the initial 30 s, and the value obtained was 156 mg/g (81%). After that, until 30 min, the q_t (sorption capacity in time) presented a small increase and it stabilized at 169 mg/g (88%). After 30 min, the q_t showed a slight variation (171–181 mg/g), indicating rapid interactions between adsorbent and adsorbate, which confer to the system a shorter

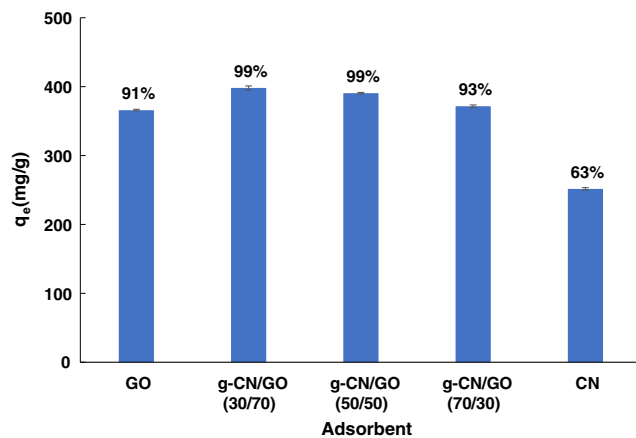


Fig. 9 Variation of percentage composition of materials. Adsorbent dosage 0.05 g/L (1.25 mL). BB26 dye initial concentration of 200 mg/L (3.75 mL), agitation of 150 oscillations/min, pH 6, under 2-min ultrasonic time, and at room temperature

equilibrium time when compared with other adsorbents (Alkan and Gan 2002). The contact time of 30 min was considered the optimized time for the BB26 removal by the CN/GO nanocomposite.

Variation in the adsorbent dose

The variation of the nanocomposite CN/GO 50/50 concentration was evaluated in the range of 0.05–0.4 g/L (Fig. 11). The increase in concentration improved the BB26 removal efficiency due to the greater availability of sites for adsorption in the CN/GO nanocomposite.

When the adsorbent dose was 0.05 g/L, we observed a greater q_e (699 mg/g). The adsorbent dose of 0.3 and 0.4 g/L removed 99% of the BB26 dye; however, low q_e was observed (339 and 244 mg/g, respectively). It is important to mention that the concentration of 0.1 g/L resulted in a q_e of 649 mg/g and had an efficiency of 63%, being characterized

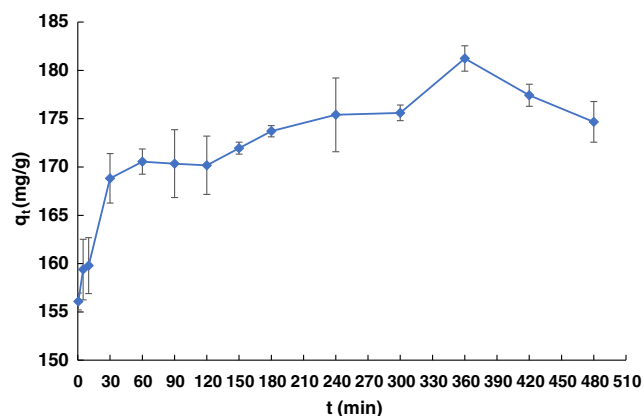


Fig. 10 Variation of BB26 uptake with contact time. Nanocomposite dosage 0.5 g/L (7.5 mL). BB26 initial concentration 100 mg/L (22.5 mL), agitation 150 oscillations/min, pH 6, under 2 min of sonication, and at room temperature

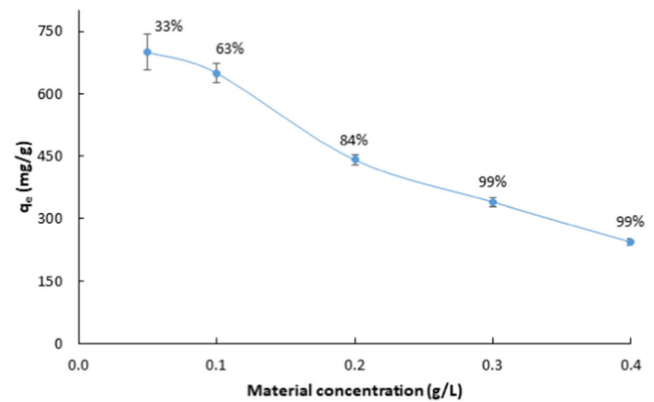


Fig. 11 Variations of CN/GO nanocomposite (50/50) dose. Nanocomposite dosage of 0.05–0.4 g/L (0.125–1.000 mL). BB26 dye initial concentration of 100 mg/L, agitation 150 oscillations/min during 30 min, at pH 6, under 2-min ultrasonic time, and at room temperature

as an ideal scenario to be used in the optimization process considering q_e and percentage of dye removal.

Sonication time variation

Sonication is an indispensable tool for the complete dispersion of the adsorbent material in water and improves efficiency in the adsorption process. Akbari Dehkharghani (2019) compared the performance of the 3-h exfoliated CN with that of the non-exfoliated CN for metal removal and concluded that exfoliated CN had better efficiency. According to the author, the sonication improved the material surface contact area, and, as a result, it enhanced the chemical interactions between the metallic cations and the amino groups of the adsorbent. Regarding graphene adsorbents, sonication is responsible for improving the graphene dispersion and breaking graphene sheets, thus increasing its surface area (Ye and Feng 2016). However, prolonged sonication drastically reduces their sheet size, negatively altering graphene mechanical characteristics.

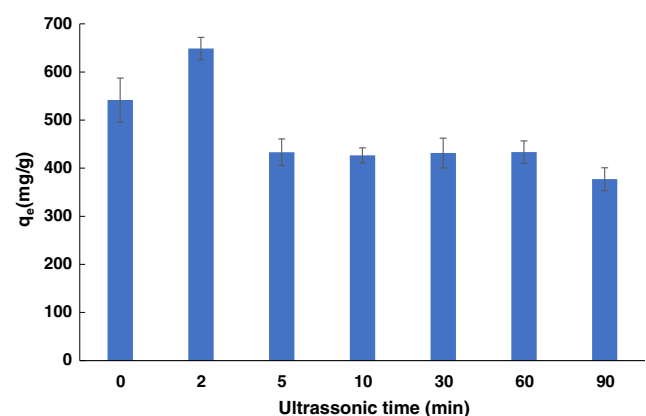


Fig. 12 Variation of ultrasonic assistance time on BB26 dye removal. CN/GO adsorbent dosage 0.1 g/L (0.25 mL), BB26 initial concentration 100 mg/L (4.75 mL), agitation 150 oscillations/min during 30 min, at pH 6, under 0–90 min of sonication, and at room temperature

Sonication was applied before the adsorption process to evaluate its influence in the BB26 uptake (Fig. 12). In the absence of ultrasonic assistance, the removal efficiency was 542 mg/g. However, when we applied sonication for 2 min, the BB26 dye adsorption onto the nanocomposite improved to 649 mg/g, because short sonication time enhanced the composite dispersibility in water and the breakage of sheets increases its superficial area, which is responsible for improving adsorption. Increasing the sonication time did not improve the process further, and the adsorption efficiency was reduced and ranged from 433 to 377 mg/g (after 90 min). Le et al. (2019) reported that extended sonication time caused the loss of oxygen-containing groups and an increase in defects on graphene nanosheets, which weaken the π - π interactions between adsorbent and adsorbate. The intense breakage of GO sheets guides the adsorption efficiency of the material, considering that after 2 min of sonication the sorption efficiency decreased, showing that graphene sheets had its mechanical properties affected.

Effect of the temperature

Evaluating the behavior of the process at different temperatures is relevant for determining the best conditions to remove the pollutant, as well as the main characteristics of the process. The influence of temperature on the BB26 adsorption process is illustrated in Fig. 13. At a higher temperature, the adsorption rate descended. Therefore, the best result obtained was at the temperature of 298 K (25 °C), corresponding to a q_e of 649 mg/g (63%).

The Brownian movement of the particles increases with the temperature rise, to the point of interfering with the electrostatic and π - π interactions between adsorbent and adsorbate. As a result, smaller floccules (He et al. 2013) are generated. This behavior, according to the temperature variation, reveals the exothermic nature of the adsorption. An endothermic

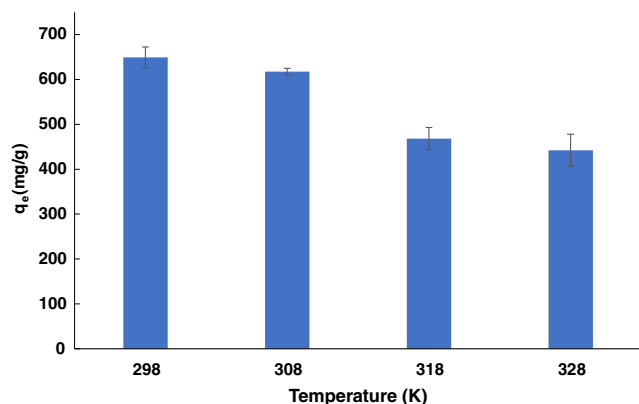


Fig. 13 Temperature variation. GO/CN adsorbent dosage 0.1 g/L (0.25 mL), BB26 initial concentration 100 mg/L (4.75 mL), agitation 150 oscillations/min during 30 min, pH 6, under 2 min of sonication, and temperature between 298 and 328 K

adsorption is characterized by energy consumption, while in exothermic reaction, there is heat release.

Effect of initial BB26 dye concentration

The plot of the BB26 removal capacity by the nanocomposite CN/GO 50/50 versus dye concentration is presented in Fig. 14. The results show that with an increase in the initial BB26 concentration, the dye uptake also increased, until 649 mg/g, when BB26 concentration was 100 mg/L. This can be attributed to the high number of active sites available in the adsorbent. Afterwards, the adsorption reached a plateau between 100 and 300 mg/L of BB7 concentration and at 375 mg/L resumed growth, reaching a high removal capacity (917 mg/g). The presence of a plateau followed by an inflection point suggests an increase in the number of available active sites for BB26 attachment when the initial dye concentration increased (Rodríguez et al. 2019). This behavior is frequently associated with multilayer adsorption (Giles et al. 1974).

Effect of pH

The pH of the dye solution is an important factor for the adsorption process assessment. Variations on pH affect the degree of dye ionization and electrical charge of adsorbent materials and thus affecting electrostatic interactions (Wang et al. 2010).

BB26 has a pKa of 8.3 (de Souza et al. 2019), and when $\text{pH} < \text{pKa}$, the dye is ionized with the predominance of its cationic species, while at $\text{pH} > \text{pKa}$, there is a predominance of its negative species (de Souza et al. 2019). More specifically, at pH 2, the main BB26 species present in the solution have two protonated amine groups, which represent ~ 96% of the total of species (Specie 2, red line, Fig. 15) (Chemicalize was used for predictions of pKa properties). With a pH below 4, the quantity of the specie that has 3 amine groups protonated

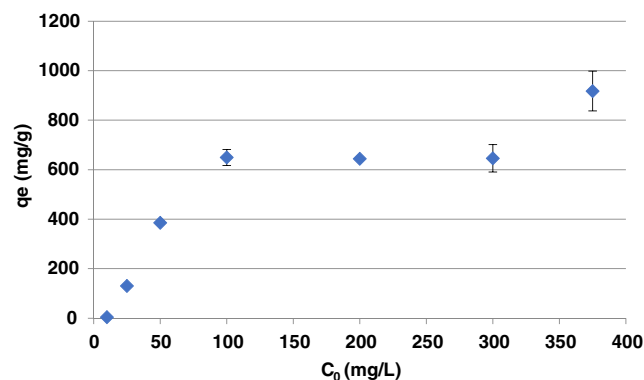


Fig. 14 Variation of BB26 initial concentration. CN/GO adsorbent dosage 0.1 g/L, BB26 initial concentration (10–375 mg/L), agitation 150 oscillations/min until equilibrium, pH 6, under 2 min of sonication at 298 K

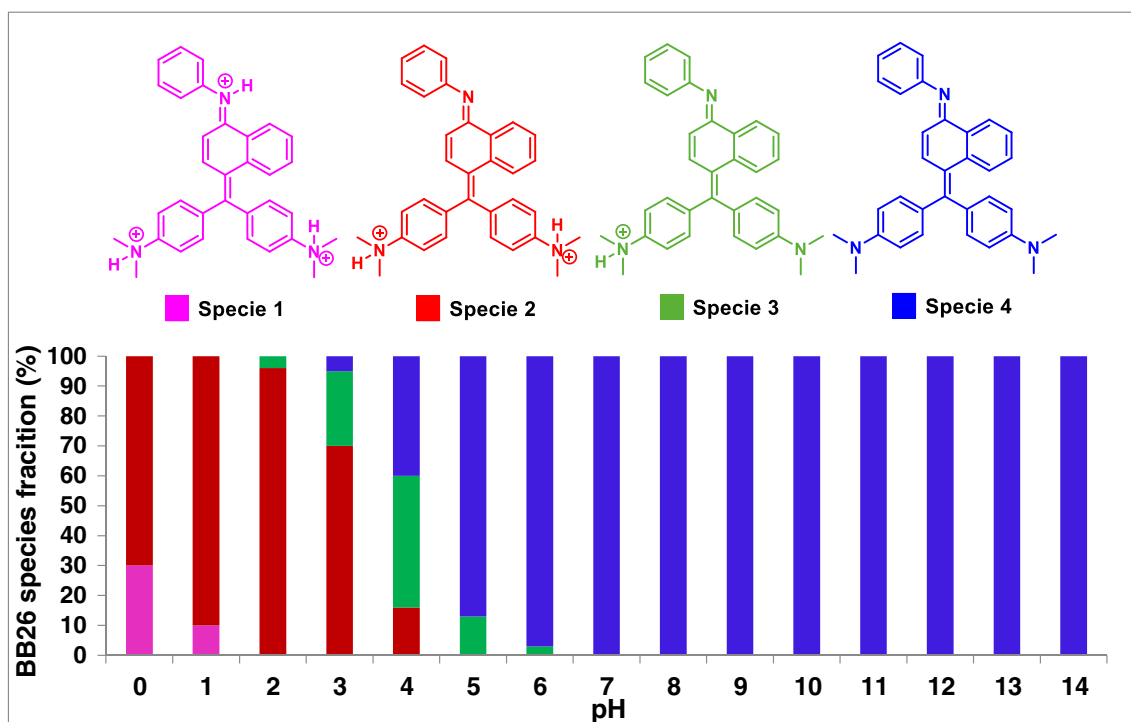


Fig. 15 BB26 microspecies distribution according to pH variation. Data obtained from Chemicalize (2019)

gradually increases with the pH reduction, reaching ~30% of total species at pH zero (Fig. 15).

In addition, the surface charge of the adsorbent material at different pH concentrations can be obtained by zeta potential measurements. These were performed at the pH range of 4 to 10 for the nanocomposite as well as the pristine GO and CN. The results indicate that the material surface is negatively charged in the whole pH spectrum evaluated, with zeta potential ranging between -16 and -45 mV (Fig. 16).

We carried out BB26 removal experiments with a pH range of 2–10. At pH 12, the dye formed lumps and did not dissolve. At pH above 10, the dye suffered changes in its basic characteristics, mainly in coloration, acquiring a grayish tone (Fig. 17). Kataria et al. (2016) observed the same color change in BB26 dye in a solution with pH 10.

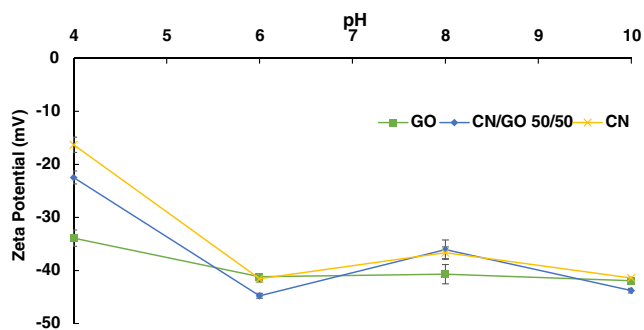


Fig. 16 Zeta potential of GO, CN, and GO/CN nanocomposite at pH 4–10

At pH 10 and 8, the adsorbent had the lowest BB26 uptake performance, with a q_e of 182 and 359 mg/g, respectively. This probably occurs due to the absence of protonated amine groups (Chemicalize was used for predictions of pKa properties). At pH 6 and 4, the q_e was 649 and 571 mg/g, respectively. We observed, as shown in Fig. 15, that the BB26 Specie 3, with one protonated amine group, begins to appear at pH 6 and at pH 4, and that there are Species 2 with two protonated amine groups and a higher level of Specie 3. This justifies the efficiency removal observed at acidic conditions. At pH 6, 97% of dye molecules are in the neutral form (Specie 4); thus, above this pH, π - π interactions are the main mechanism, once CN/GO and BB26 have planar aromatic lattices that allow these interactions. As the pH decreases, the presence of protonated amine groups increases, as well as the removal efficiency. The highest removal efficiency occurred at pH 2 (Fig. 18), with a q_e of 920 mg/g. This probably happens because BB26 is highly positively charged at a low pH, which contributes to electrostatic interactions between negatively charged adsorbent and positively charged dye surface (Zhang et al. 2014a). The following experiments were carried out at pH 2.

Kinetics of removal

The adsorption process undergoes several stages. Studying how the adsorption process occurs and which step determines the velocity of this process is essential to understand the interaction dynamics between sorbent and sorbate as well as to

Fig. 17 BB26 in water solution, pH range 2–10. Concentration of 100 mg/L. Room temperature



determine the amount of mass to be adsorbed and the time required. Finding the optimal parameters is also indispensable for applying the process in full scale (Melo et al. 2014).

The sorption kinetics was assessed using non-linearized models of pseudo-first-order (Lagergren 1898; Moussout et al. 2018), pseudo-second-order (Aazza et al. 2018; Ho and Mckaf 2000; Lin and Wang 2009), and intraparticle diffusion (Weber and Morris 1963). Kinetic models of the pseudo-first-order, pseudo-second-order, and intraparticle diffusion are expressed by Eqs. 3, 4, and 5, where k_1 (min^{-1}), k_2 (g/mg min), and k_3 ($\text{mol/g min}^{0.5}$) are constants that express the adsorption rate in each model.

$$q_t = q_e (1 - e^{-k_1 t}) \tag{3}$$

$$q_t = \frac{k_2 \cdot q_e^2 t}{1 + k_2 q_e t} \tag{4}$$

$$q_t = K q_e^{0.5} + C \tag{5}$$

q_e (mg/g) is the dye quantity adsorbed per g of the adsorbate at equilibrium, q_t (mg/g) is the adsorption capacity in time, and t is the time (min).

The pseudo-first-order model obtained a R^2 of 0.9745 to 0.9853 (Table 1). The theoretical values of q_e are close to the experimental data, which indicates that the model represents the data fitted consistently. Considering the intraparticle diffusion model, the correlation coefficient ranged from 0.3201 to 0.3893, revealing the inadequacy of the model for the

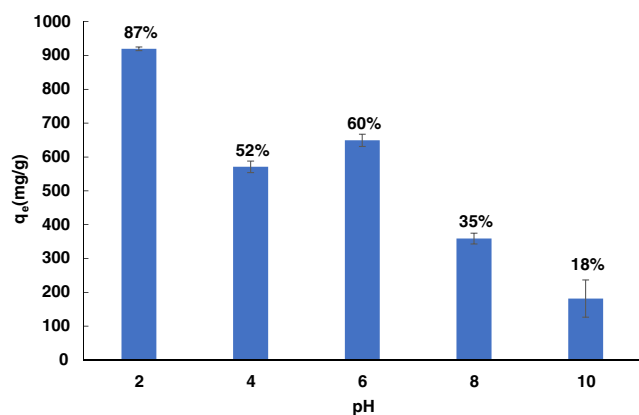


Fig. 18 pH variation. GO/CN adsorbent dosage 0.1 g/L (0.25 mL), BB26 initial concentration 100 mg/L (4.75 mL), agitation 150 oscillations/min during 30 min, under 2 min of sonication, and 298 K

studied adsorption process. Also, the rate constants obtained are unrealistic to express experimental data. The model that dictates the velocity of the process in this study was the pseudo-second-order model, since it provided higher correlation coefficients than the pseudo-first-order model. In addition, the theoretical q_e was very close to the experimental data. The range of the correlation coefficient was 0.9813 to 0.9987. In review of the adsorption of dyes in water, Yagub et al. (2014) state that most adsorption processes fitted better with the pseudo-second-order model, because, in general, the pseudo-first-order model makes a good representation of the adsorption process after 20 and 30 min—the intraparticle diffusion model is also strictly representative. On the other hand, the pseudo-second-order model applies to the entire time spectrum of the process (Ho and Mckay 1998, 1999).

Adsorption isotherm study

For a better understanding of the interaction processes between adsorbents and adsorbates, we applied isothermal studies (Table 2). The experimental data was compared with the studies performed by Giles, and five isothermal models were used: Langmuir, Freundlich, Temkin, Redlich–Peterson, and Dubinin–Radushkevich. One of the first analyses to be performed is about the format that the isotherm presents in the plot of the adsorbed BB26 dye amount (per gram) of the adsorbate (mg/L) versus the dye concentration, C_e (mg/L), both at equilibrium. The BB26 dye concentration used in these experiments were between 10 and 375 mg/L, and the results are shown in Fig. 19.

The isotherm curve (Fig. 19) of the adsorption of BB26 on nanocomposite CN/GO 50/50 grows in a convex form reaching a plateau with an equilibrium concentration of 24 mg/L. Then, the curve grows exponentially, reaching a remarkable adsorption capacity of BB26 uptake (3510 mg/g—94%). This behavior corresponds to the L3 type isotherm and indicates the adsorption in multilayers (Giles et al. 1974).

The Langmuir isotherm

The Langmuir isotherm model assumes that the adsorption process occurs in a specific number of homogeneous sites. The sites can only support one molecule, and thus with no

Table 1 Fitted parameters of BB26 adsorption kinetics for CN/GO

		BB26 concentration (mg/L)				
		10	50	100	200	300
Experimental q_e		44.1102	478.0340	950.9134	1754.8780	2761.5521
Pseudo-first order	k^{-1} (min ⁻¹)	4.8760	4.7560	4.3850	4.3760	4.2826
	q_e (mg/g)	46.4000	486.600	981.8082	1769.6102	2768.0300
	R^2	0.9809	0.9853	0.9745	0.9820	0.9811
Pseudo-second order	k^{-1} (min ⁻¹)	0.4876	0.3980	0.3569	0.3876	0.0238
	q_e (mg/g)	46.4003	486.6040	981.8090	1825.0339	2787.5200
	R^2	<i>0.9813</i>	<i>0.9985</i>	<i>0.9958</i>	<i>0.9987</i>	<i>0.9984</i>
Intraparticle diffusion	k^{-1} (mg/(g min ^{1/2}))	5.0662	55.6514	152.1173	206.0092	323.6568
	C	25.1103	256.5876	469.9929	923.4269	1440.6251
	R^2	0.3201	0.3534	0.3893	0.3664	0.3697

Italicized values are the highest R^2

additional adsorption on them (Langmuir 1918). In the following model, K_L and q_L are the Langmuir isothermal constants.

$$q_e = \frac{q_L \cdot K_L \cdot C_e}{1 + K_L \cdot C_e} \tag{6}$$

where q_e is the amount of adsorbed dye per gram of the adsorbent at equilibrium (mg/g), q_L is the maximum adsorbent

capacity (mg/g), K_L is the constant adsorbent/adsorbent interaction (L/mg), and C_e is the adsorbate concentration at equilibrium (mg/L) (Dada et al. 2012).

The Freundlich isotherm

This model is one of those that relate the quantity of adsorbed material and the material concentration in the solution from empiric data. The isotherm is applied to the adsorption on heterogeneous surfaces, and it is not restricted to the formation of monolayer. The model is expressed in Eq. 7 (Freundlich 1906):

$$q_e = K_F \cdot C_e^{\frac{1}{n}} \tag{7}$$

where q_e is the dye concentration adsorbed at equilibrium per unit of adsorbent (mg/g), C_e is the dye concentration in solution at equilibrium (mg/L), K_f is the Freundlich constant [mg^{1-(1/n)} · L^(1/n)/g], and $1/n$ is the sorption intensity (Senthil

Table 2 Adsorption parameters calculated from non-linear isotherm models

Isotherm model	Parameters	Values
Langmuir	k_L (L/mg)	-
	q_m (mg/g)	-
	R^2	< 0.9000
	ARE	-
Freundlich	k_F ((mg/g)(L/mg) ^{1/n})	3.1797
	1/n (dimensionless)	1.9986
	R^2	0.9743
	ARE	4.5422
Temkin	k_T (L/g)	0.1706
	RT/b	1904.1583
	R^2	0.9437
	ARE	8.2354
Redlich–Peterson	k_R (L/mg)	108.2074
	a_R (L/mg) ^β	0.0615
	B	0.0167
	R^2	0.9077
	ARE	38.7312
	q_s (mg/g)	3987.4511
	K_{DR} (mol ² /kJ ²)	0.00003
Dubinin–Radushkevich	R^2	0.9839
	ARE	3.8389

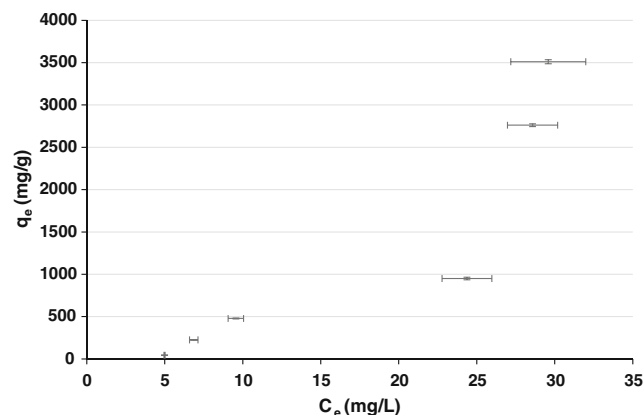


Fig. 19 Isotherm of BB26 adsorption onto CN/GO, at 298 K. BB26 concentration of 10–375 mg/L (4.75 mL), nanomaterial concentration of 0.1 g/L (0.250 mL), pH 2 under 2 min of sonication

Kumar et al. 2010). The inclination ($1/n$) allows the understanding of the adsorption process, and the range between 0 and 1 is associated with the chemisorption process. The inclination above 1 is related to the formation of multilayers (de Sá et al. 2017).

The Temkin isotherm

Temkin isotherm considers the effects of the indirect adsorbate/adsorbate interactions. As result of these interactions, the adsorption heat decreases linearly according to the increase of the surface coating degree (Vidal et al. 2011). The equation is shown in Eq. 8 (Ostrovskii 1989):

$$q_e = \frac{R.T}{b} \cdot \ln(K_T \cdot C_e) \tag{8}$$

where q_e is the amount adsorbed at equilibrium, R is the gas constant (8.314 J/mol K), T is the absolute temperature (K), b is the Temkin constant related to the sorption heat (J/mol), K_t is the Temkin isotherm constant (L/g), and C_e is the adsorbate concentration in solution at equilibrium (mg/g) (Hameed et al. 2009).

The Redlich–Peterson isotherm

This model (Redlich and Peterson 1959) is commonly used to represent the adsorption equilibrium at a wide range of concentrations, and it can be applied in homogeneous and heterogeneous systems, since it is a hybrid isotherm based on the Langmuir and Freundlich isotherms (Foo and Hameed 2010). The isotherm incorporates three parameters in an empirical equation (Eq. 9):

$$q_e = \frac{k_R \cdot C_e}{1 + a_R \cdot C_e^\beta} \tag{9}$$

where q_e is the amount adsorbed at equilibrium; C_e is the adsorbate concentration in solution at equilibrium (mg/g); and k_R (L/mg), a_R (L/mg) $^\beta$, and β (varies from 0 to 1) are the parameters of the Redlich–Peterson isotherm. At the limit, the Redlich–Peterson isotherm approaches the Langmuir isotherm at low adsorbate concentrations, where the value β is close to 1. When β is close to 0, the isotherm approaches Freundlich at high adsorbate concentrations (Wu et al. 2010).

The Dubinin–Radushkevich

The Dubinin–Radushkevich (D–R) adsorption isotherm is an empirical model that can be applied to define the adsorption processes that occur on homogeneous and heterogeneous surfaces through pore-filling mechanisms (Dubinin 1959). The non-linear form of the model is presented in Eq. 10:

$$q_e = q_s \exp(-K_{DR} \varepsilon^2) \tag{10}$$

where q_e is the amount adsorbed at equilibrium (mg/g), q_s is the maximum adsorption capacity (mg/g), and K_{DR} is the activity coefficient related to the mean free energy of adsorption (mol²/J²). This isotherm model is commonly used to determine the mean free energy ($E = 1/\sqrt{2K_{DR}}$), which can be calculated using the K_{DR} isothermal constant. The determination of the mean free energy depends on the K_{DR} units and Polanyi potential (ε) from which the D–R equation derives. Polanyi’s potential can be calculated using Eq. 11:

$$\varepsilon = RT \ln \left(1 + \frac{1}{C_e} \right) \tag{11}$$

where R is the gas constant (8.314 J/kmol), T is the absolute temperature (K), and C_e is the equilibrium concentration in mg/L or mol/L (Satilmis 2020). However, Hu and Zhang (2019) showed that the potential of Polanyi calculated through C_e is not correct, since the logarithmic term must be dimensionless. Thus, the mean free energy was not calculated.

The quality of the adjustment was verified according to the coefficient of determination (R^2) and average relative error (Li and Zhao 2005), according to Eq. 12:

$$ARE = \frac{100}{N} \sum_{i=1}^N \left[\frac{q_{e,cal} - q_{e,meas}}{q_{e,meas}} \right]_i \tag{12}$$

Considering the determination coefficients, the most adequate model to describe the results obtained is the Dubinin–Radushkevich ($R^2 = 0.9829$) followed by the Freundlich ($R^2 = 0.9743$), Temkin ($R^2 = 0.9437$), Redlich–Peterson ($R^2 = 0.9077$), and Langmuir ($R^2 < 0.9000$) models (Table 2). This sequence was established by observing errors related to isotherms. Langmuir, Redlich–Peterson, and Temkin curves have high relative errors associated. Therefore, it would be inaccurate to analyze the parameters displayed in these isotherms. The D–R equation has a maximum theoretical adsorption capacity of 3987 mg/g, and the Freundlich sorption

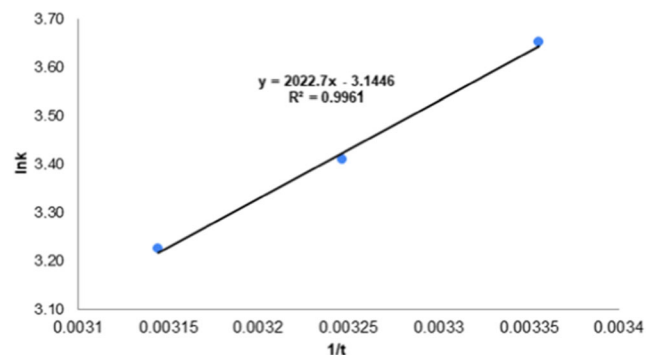


Fig. 20 Fitting of the adsorption thermodynamic parameters of BB26 by CN/GO

Table 3 Thermodynamic parameters of the BB26 adsorption at 298 K, 308 K, and 318 K

R^2	ΔG (KJ/mol)			ΔH (KJ/mol)	ΔS (KJ/mol)
	298 K	308 K	318 K		
0.99	-9.0444	-8.7251	-8.5240	-16.8192	-0.0261

intensity constant ($1/n$) determined (1.9986) was higher than 1, indicating multilayer formation.

Thermodynamic parameters

The free energy change (ΔG), enthalpy change (ΔH), entropy change (ΔS), and the adsorption equilibrium constant can be calculated according to the derivations of Gibbs free energy relations and van't Hoff equations (Lee et al. 2015), as shown in Eqs. 13 and 14.

$$\Delta G = -R.T.\ln K \quad (13)$$

$$\ln K = \frac{\Delta S}{R} - \frac{\Delta H}{R.T} \quad (14)$$

where ΔG is the Gibbs free energy (J/mol), ΔH is the enthalpy change (J/mol), ΔS is the entropy change (J/mol), R is the universal gas constant (8.314 J/Kmol), and T is the temperature (K). ΔH and ΔS are calculated by using the slope and intercept, respectively, from fitting $\ln K$ versus $(1/T)$ (Fig. 20).

The thermodynamic parameters are shown in Table 3.

The variation of the free energy (ΔG) was from -9.04 at 298 K to -8.52 kJ/mol at 318 K. The ΔG values become less negative as the temperature rises, which indicates that the removal occurred more easily at lower temperatures (Wang

et al. 2015). The sign of ΔG predicts the main mechanism of adsorption in the dye removal process. In the range of -20 to 0 kJ/mol, there is mainly physisorption, while from -80 to -400 kJ/mol, the dominant process is chemisorption (Gamoudi and Srasra 2019). Therefore, looking for a ΔG value from -9.04 to -8.52 kJ/mol, we concluded that the main mechanism in the process was physisorption, that is, electrostatic attraction and π - π interactions between sorbent and sorbate (Carrier et al. 2012; Sims et al. 2019). These data corroborate the discussions based on the zeta potential of the adsorbent material and ionization of BB26. Figure 21 shows the main adsorption interactions between CN/GO nanocomposites and BB26 dye.

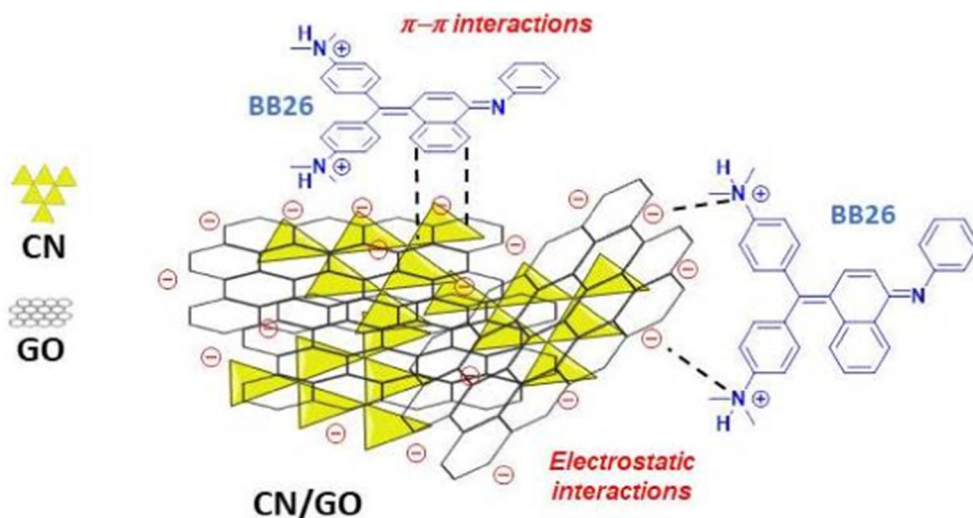
Moreover, the negative enthalpy change means that it is an exothermic reaction, and this is in accordance with the data collected for the removal performed in relation to temperature variation (Cheruiyot et al. 2019). On the other hand, the negative entropy change indicates that there was less disorder or randomness at the CN/GO interface covered by BB26 dye (Sumalinog et al. 2018).

Recycling tests

The recycling step is an important parameter to select an adsorbent material because it interferes in the usability, efficiency, and consequently cost of the process (Ren et al. 2018). In this context, five adsorption/desorption cycles were carried out with the nanocomposite CN/GO 50/50 to verify the reuse limit of the material, without significant loss of efficiency.

Organic solvents have proven to be a good option when it comes to recycling materials that contain CN (Cheruiyot et al. 2019; Sumalinog et al. 2018). In this regard, ethanol was chosen to be used in the desorption step. After the BB26 adsorption tests, the adsorbent material was washed with ultrapure

Fig. 21 Proposed adsorption interactions between CN/GO nanocomposites and BB26 dye



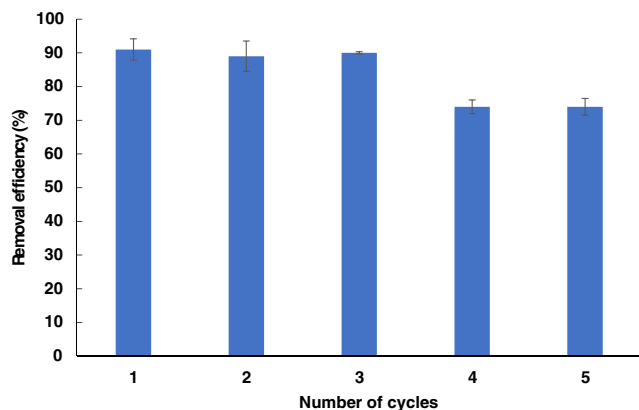


Fig. 22 Reusability study of CN/GO (50/50)

water and ethanol twice. After washing, the material was used in another cycle.

Figure 22 shows that up to the third cycle, the BB26 uptake efficiency remained approximately constant, with values of 89% in the second test and 90% in the third. In the fourth cycle, the performance fell 16% in relation to the third cycle and remained the same in the fifth cycle. Even falling to 74% in the last two adsorption tests, the removal efficiency was satisfactory in the five test cycles, showing one of the advantages of using CN/GO nanocomposite as an adsorbent material.

The values obtained from the maximum BB26 uptake by the adsorption onto the nanocomposite CN/GO (q_{max}) at pH 6 and 2 were compared with other materials described in the literature as shown in Table 4. In neutral ultrapure water pH, the BB26 uptake efficiency was 917.78 mg/g, which is 5.6 times higher than the highest previously reported value (Kataria et al. 2016). This result indicates that CN/GO composites are potential basic dye-filtering agents at environmental conditions. At pH 2, BB26 removal by CN/GO reached a remarkable value of 3510.68, being 21 times higher than those reported elsewhere (Table 4).

Conclusions

GO has been widely used in adsorption processes to remove pollutants from water, whereas carbon nitride has been poorly explored as adsorbent, as it is mainly used in catalysis reactions. In this study, we prepared pristine materials and nanocomposites and characterized them by using FTIR, Raman, AFM, SEM, TEM, XRD, and zeta potential techniques. The characterizations confirmed the successful preparation of GO and CN materials. After testing pure GO and CN and 30/70, 50/50, and 70/30 (CN/GO) nanocomposites, we selected nanocomposite 50/50 as the best adsorbent for removing BB26 dye from water.

The BB26 dye adsorption optimization process showed that the equilibrium was reached in 30 min at 298 K, at pH 2 and with 2 min of sonication. At high BB26 dye concentration, CN/GO composite reached a remarkable removal capacity of 3510 mg/g. Also, at natural ultrapure water, the adsorption efficiency was 917 mg/g, indicating CN/GO nanocomposites as potential dye-filtering agents at environmental conditions.

The sorption process was best described by using the Dubinin–Radushkevich isotherm and kinetics by using the pseudo-second-order model. The sorption process was thermodynamically spontaneous and exothermic in nature. The main sorption mechanism was physisorption, that is, the sorbent and sorbate molecules interact mainly by electrostatic attractions and π – π interactions.

Recycling tests showed that after 5 cycles of sorption/desorption, the CN/GO nanocomposite maintained an optimum level of efficiency, and this application can be extended to remove other cationic dyes without significant loss of efficiency. The results showed that CN/GO nanocomposite had high adsorption capacity when compared with pure materials and other adsorbents, indicating that this material is viable for industrial wastewater treatment in acidic or neutral conditions.

Table 4 Comparative data of BB26 removal by other materials

Adsorbent material	Removal capacity (mg/g)	pH	Reference
Fly ash	0.024	8.0	Khare et al. 1987
Carbon/Ba/alginate beads	1.94	4.0	Kumar et al. 2013
Activated carbon (AC1-R1)	73.00	5.8	de Souza et al. 2018
Activated carbon (AC2-R2)	13.00	5.8	de Souza et al. 2018
Activated carbon (AC3-R2)	76.00	5.8	de Souza et al. 2018
Iron-doped titanium/silane	153.89	6.5	Anirudhan et al. 2014
Zinc oxide nanoparticles	163.93	6.0	Kataria et al. 2016
H ₃ PO ₄ -activated carbons (AC-R1)	48.58	5.8	de Souza et al. 2019
H ₃ PO ₄ -activated carbons (AC-R2)	51.11	5.8	de Souza et al. 2019
Porous CN/GO nanocomposites	917.78	6.0	This work
Porous CN/GO nanocomposites	3510.68	2.0	This work

Acknowledgments This research was supported by LNBR – Brazilian Biorenewables National Laboratory (CNPEM/MCTIC) during the use of the characterization of macromolecule (MAC) equipment open access facility. The authors thank Prof. Dr. Carlos Roque Duarte Correia for allowing us to use his laboratory facilities and Espaço da Escrita—Coordenadoria Geral da Universidade—UNICAMP—for the language services provided.

Authors' contributions Junia Teixeira Martins: conceptualization, original draft preparation, writing review, methodology, performing the experiments, formal analysis, and investigation. Carlos Henrique Guimarães: conceptualization, performing the experiments, original draft preparation, writing review, methodology, formal analysis, and investigation. Paula Mayara Silva: methodology, performing the experiments, writing, and formal analysis. Rafael L. Oliveira: methodology, performing the experiments, writing, and formal analysis. Patricia Prediger: conceptualization, writing review, methodology, formal analysis, investigation, resources, and funding acquisition.

Funding We thank the Research Supporting Foundation of the State of São Paulo (FAPESP, proposal n°. 2019/07822-2), Research and Extension Supporting Fund of the University of Campinas (FAPEX), Coordination for the Improvement of Higher Education Personnel (CAPES, Financial code – 001), and National Council for Scientific and Technological Development (CNPq).

Data availability Not applicable.

Compliance with ethical standards

Conflict of interest The authors declare that they have no conflict of interest.

Ethical approval Not applicable.

Consent to participate Not applicable.

Consent for publication Not applicable.

References

- Aazza M, Ahlafi H, Moussout H, Maghat H (2018) Adsorption of methanitrophenol onto alumina and HDTMA modified alumina: kinetic, isotherm and mechanism investigations. *J Mol Liq* 268:587–597. <https://doi.org/10.1016/j.molliq.2018.07.095>
- Akbari Dehkharghani A (2019) Exfoliated Graphitic carbon nitride for the fast adsorption of metal ions from acid mine drainage: a case study from the Sungun copper mine. *Mine Water Environ* 38:335–341. <https://doi.org/10.1007/s10230-018-0561-x>
- Alkan M, Gan MDO (2002) The removal of Victoria blue from aqueous solution by adsorption on a low-cost material. *Adsorption* 8:341–349
- Allen SJ, McKay G, Porter JF (2004) Adsorption isotherm models for basic dye adsorption by peat in single and binary component systems. *J Colloid Interface Sci* 280:322–333. <https://doi.org/10.1016/j.jcis.2004.08.078>
- Al-Zboon KK (2018) Phosphate removal by activated carbon–silica nanoparticles composite, kaolin, and olive cake. *Environ Dev Sustain* 20:2707–2724. <https://doi.org/10.1007/s10668-017-0012-z>
- Anirudhan TS, Divya PL, Nima J, Sandeep S (2014) Synthesis and evaluation of iron-doped titania/silane based hydrogel for the adsorptional photocatalytic degradation of Victoria blue under visible light. *J Colloid Interface Sci* 434:48–58. <https://doi.org/10.1016/J.JCIS.2014.07.030>
- Belpaire C, Reyns T, Geeraerts C, Van Loco J (2015) Toxic textile dyes accumulate in wild European eel *Anguilla anguilla*. *Chemosphere* 138:784–791. <https://doi.org/10.1016/j.chemosphere.2015.08.007>
- Burrow JN, Pender JP, Guerrero JV, Wygant BR, Eichler JE, Calabro DC, Mullins CB (2020) CaCl₂-activated carbon nitride: hierarchically nanoporous carbons with ultrahigh nitrogen content for selective CO₂ adsorption. *ACS Appl Nano Mater* 3:5965–5977. <https://doi.org/10.1021/acsnm.0c01112>
- Carrier M, Hardie AG, Uras Ü, Görgens J, Knoetze J(H) (2012) Production of char from vacuum pyrolysis of South-African sugar cane bagasse and its characterization as activated carbon and bio-char. *J Anal Appl Pyrolysis* 96:24–32. <https://doi.org/10.1016/j.jaap.2012.02.016>
- ChemAxon Ltd. (2019) Chemicalize. <https://chemaxon.com/products/chemicalize>. Accessed 23 Mar 2020
- Chen KT, Lu CS, Chang TH, Lai YY, Chang TH, Wu CW, Chen CC (2010) Comparison of photodegradative efficiencies and mechanisms of Victoria blue R assisted by nafion-coated and fluorinated TiO₂ photocatalysts. *J Hazard Mater* 174:598–609. <https://doi.org/10.1016/j.jhazmat.2009.09.094>
- Chen R, Zhang J, Wang Y, Chen X, Zapien JA, Lee CS (2015) Graphitic carbon nitride nanosheet@metal-organic framework core-shell nanoparticles for photo-chemo combination therapy. *Nanoscale* 7: 17299–17305. <https://doi.org/10.1039/c5nr04436g>
- Chen CY, Wang GH, Tseng IH, Chung YC (2016) Analysis of bacterial diversity and efficiency of continuous removal of Victoria blue R from wastewater by using packed-bed bioreactor. *Chemosphere* 145:17–24. <https://doi.org/10.1016/j.chemosphere.2015.11.061>
- Cheruiyot GK, Wanyonyi WC, Kiplimo JJ, Maina EN (2019) Adsorption of toxic crystal violet dye using coffee husks: equilibrium, kinetics and thermodynamics study. *Sci Afr* 5:e00116. <https://doi.org/10.1016/j.sciaf.2019.e00116>
- Dada AO, Lalekan AP, Olatunya AM, DADA O (2012) Langmuir, Freundlich, Temkin and Dubinin–Radushkevich isotherms studies of equilibrium sorption of Zn²⁺ onto phosphoric acid modified rice husk. *IOSR J Appl Chem* 3:38–45. <https://doi.org/10.9790/5736-0313845>
- de Figueiredo Neves T, Barticiotto Dalarme N, da Silva PMM et al (2020a) Novel magnetic chitosan/quaternary ammonium salt graphene oxide composite applied to dye removal. *J Environ Chem Eng* 8:103820. <https://doi.org/10.1016/j.jece.2020.103820>
- de Figueiredo Neves T, Kushima Assano P, Rodrigues Sabino L et al (2020b) Influence of adsorbent/adsorbate interactions on the removal of cationic surfactants from water by graphene oxide. *Water Air Soil Pollut* 231. <https://doi.org/10.1007/s11270-020-04669-w>
- de Sá A, Abreu AS, Moura I, Machado AV (2017) FREUD.pdf. *Water Purif* 289–322. <https://doi.org/10.1016/B978-0-12-804300-4.00008-3>
- de Souza TNV, de Carvalho SML, Vieira MGA, da Silva MGC, Brasil DSB (2018) Adsorption of basic dyes onto activated carbon: experimental and theoretical investigation of chemical reactivity of basic dyes using DFT-based descriptors. *Appl Surf Sci* 448:662–670. <https://doi.org/10.1016/j.apsusc.2018.04.087>
- de Souza TNV, Vieira MGA, da Silva MGC et al (2019) H₃PO₄-activated carbons produced from açai stones and Brazil nut shells: removal of basic blue 26 dye from aqueous solutions by adsorption. *Environ Sci Pollut Res* 26. <https://doi.org/10.1007/s11356-019-04215-0>
- Desipio MM, Van Bramer SE, Thorpe R, Saha D (2019) Photocatalytic and photo-fenton activity of iron oxide-doped carbon nitride in 3D printed and LED driven photon concentrator. *J Hazard Mater* 376: 178–187. <https://doi.org/10.1016/J.JHAZMAT.2019.05.037>

- Ding F, Li XN, Diao JX, Sun Y, Zhang L, Ma L, Yang XL, Zhang L, Sun Y (2012) Potential toxicity and affinity of triphenylmethane dye malachite green to lysozyme. *Ecotoxicol Environ Saf* 78:41–49. <https://doi.org/10.1016/j.ecoenv.2011.11.006>
- Dubinin MM (1959) The potential theory of adsorption of gases and vapors $w \sim K_i$). 235–241. <https://doi.org/10.1021/cr60204a006>
- Eftekhari A, Fan Z (2017) Ordered mesoporous carbon and its applications for electrochemical energy storage and conversion. *Mater Chem Front* 1:1001–1027. <https://doi.org/10.1039/c6qm00298f>
- Foo KY, Hameed BH (2010) Insights into the modeling of adsorption isotherm systems. *Chem Eng J* 156:2–10. <https://doi.org/10.1016/j.cej.2009.09.013>
- Freundlich H (1906) Über die adsorption in lösungen. *Z Phys Chem* 57U: 385–470
- Gamoudi S, Srasra E (2019) Adsorption of organic dyes by HDPy+ modified clay: effect of molecular structure on the adsorption. *J Mol Struct* 1193:522–531. <https://doi.org/10.1016/j.molstruc.2019.05.055>
- Gao D, Liu Y, Liu P, Si M, Xue D (2016) Atomically thin B doped g-C₃N₄ nanosheets: high-temperature ferromagnetism and calculated half-metallicity. *Sci Rep* 6:1–8. <https://doi.org/10.1038/srep35768>
- Giles CH, Smith D, Huitson A (1974) A general treatment and classification of the solute adsorption isotherm. I. Theoretical. *J Colloid Interface Sci* 47:755–765. [https://doi.org/10.1016/0021-9797\(74\)90252-5](https://doi.org/10.1016/0021-9797(74)90252-5)
- Guo S, Deng Z, Li M, Jiang B, Tian C, Pan Q, Fu H (2016) Phosphorus-doped carbon nitride tubes with a layered micro-nanostructure for enhanced visible-light photocatalytic hydrogen evolution. *Angew Chem Int Ed* 55:1830–1834. <https://doi.org/10.1002/anie.201508505>
- Gupta VK, Suhas VK (2009) Application of low-cost adsorbents for dye removal—a review. *J Environ Manag* 90:2313–2342. <https://doi.org/10.1016/j.jenvman.2008.11.017>
- Hameed BH, Salman JM, Ahmad AL (2009) Adsorption isotherm and kinetic modeling of 2,4-D pesticide on activated carbon derived from date stones. *J Hazard Mater* 163:121–126. <https://doi.org/10.1016/j.jhazmat.2008.06.069>
- He G, Zhang J, Zhang Y, Chen H, Wang X (2013) Fast and efficient removal of cationic dye using graphite oxide, adsorption, and kinetics studies. *J Dispers Sci Technol* 34:1223–1229. <https://doi.org/10.1080/01932691.2012.739946>
- Hernández-Torres J, Gutierrez-Franco A, González PG, García-González L, Hernandez-Quiroz T, Zamora-Peredo L, Méndez-García VH, Cisneros-de la Rosa A (2016) Photoluminescence and Raman spectroscopy studies of carbon nitride films. *J Spectrosc* 2016:1–8. <https://doi.org/10.1155/2016/5810592>
- Ho KS, Mckaf G (2000) The kinetics of sorption of basic dyes from aqueous solution by sphagnum moss peat. *Can J Chem Eng* 76: 822–827
- Ho YS, Mckay G (1998) The kinetics of sorption of basic dyes from aqueous solution by sphagnum moss peat. *Can J Chem Eng* 76: 822–827. <https://doi.org/10.1002/cjce.5450760419>
- Ho YS, McKay G (1999) Pseudo-second order model for sorption processes. *Process Biochem* 34:451–465. [https://doi.org/10.1016/S0032-9592\(98\)00112-5](https://doi.org/10.1016/S0032-9592(98)00112-5)
- Hu Q, Zhang Z (2019) Application of Dubinin–Radushkevich isotherm model at the solid/solution interface: a theoretical analysis. *J Mol Liq* 277:646–648. <https://doi.org/10.1016/j.molliq.2019.01.005>
- Hu L, Zheng J, Zhao K, Deng A, Li J (2018) An ultrasensitive electrochemiluminescent immunosensor based on graphene oxide coupled graphite-like carbon nitride and multiwalled carbon nanotubes-gold for the detection of diclofenac. *Biosens Bioelectron* 101:260–267. <https://doi.org/10.1016/j.bios.2017.10.043>
- Hummers WS, Offeman RE (1958) Preparation of graphitic oxide. *J Am Chem Soc* 80:1339–1339. <https://doi.org/10.1021/ja01539a017>
- Joseph S, Abraham S, Abraham T, Priyanka RN, Mathew B (2019) S-rGO modified sulphur doped carbon nitride with mixed-dimensional hierarchical nanostructures of silver vanadate for the enhanced photocatalytic degradation of pollutants in divergent fields. *Appl Surf Sci* 495:143478. <https://doi.org/10.1016/j.apsusc.2019.07.220>
- Katarina N, Garg VK, Jain M, Kadirvelu K (2016) Preparation, characterization and potential use of flower shaped zinc oxide nanoparticles (ZON) for the adsorption of Victoria blue B dye from aqueous solution. *Adv Powder Technol* 27:1180–1188. <https://doi.org/10.1016/j.apt.2016.04.001>
- Khare SK, Panday KK, Srivastava RM, Singh VN (1987) Removal of victoria blue from aqueous solution by fly ash. *J Chem Technol Biotechnol* 38:99–104. <https://doi.org/10.1002/jctb.280380206>
- Kumar M, Tamilarasan R, Sivakumar V (2013) Adsorption of Victoria blue by carbon/Ba/alginate beads: kinetics, thermodynamics and isotherm studies. *Carbohydr Polym* 98:505–513. <https://doi.org/10.1016/j.carbpol.2013.05.078>
- Lagergren S (1898) Zur Theorie der Sogenannten Adsorption Geloster Stoffe. *K Sven vetenskapsakademiens Handlingar* 24:1–39
- Langmuir I (1918) The adsorption of gases on plane surfaces of glass, mica and platinum. *J Am Chem Soc* 40:1361–1403. <https://doi.org/10.1021/ja02242a004>
- Le GTT, Chanlek N, Manyam J et al (2019) Insight into the ultrasonication of graphene oxide with strong changes in its properties and performance for adsorption applications. *Chem Eng J* 373: 1212–1222. <https://doi.org/10.1016/j.cej.2019.05.108>
- Lee SU, Jun YS, Lee EZ, Heo NS, Hong WH, Huh YS, Chang YK (2015) Selective silver ion adsorption onto mesoporous graphitic carbon nitride. *Carbon N Y* 95:58–64. <https://doi.org/10.1016/j.carbon.2015.08.012>
- Li XR, Zhao Z (2005) Relative error measures for evaluation of estimation algorithms. 2005 7th Int Conf Inf Fusion. *FUSION* 1:211–218. <https://doi.org/10.1109/ICIF.2005.1591857>
- Li M, Wang B, Yang M, Li Q, Calatayud DG, Zhang S, Wang H, Wang L, Mao B (2020) Promoting mercury removal from desulfurization slurry via S-doped carbon nitride/graphene oxide 3D hierarchical framework. *Sep Purif Technol* 239:116515. <https://doi.org/10.1016/j.seppur.2020.116515>
- Lin J, Wang L (2009) Comparison between linear and non-linear forms of pseudo-first-order and pseudo-second-order adsorption kinetic models for the removal of methylene blue by activated carbon. *Front Environ Sci Eng China* 3:320–324. <https://doi.org/10.1007/s11783-009-0030-7>
- Liu P, Zhu C, Mathew AP (2019) Mechanically robust high flux graphene oxide-nanocellulose membranes for dye removal from water. *J Hazard Mater* 371:484–493. <https://doi.org/10.1016/j.jhazmat.2019.03.009>
- Luo D, Zhang F, Ren Z, Ren W, Yu L, Jiang L, Ren B, Wang L, Wang Z, Yu Y, Zhang Q, Ren Z (2019) An improved method to synthesize nanoscale graphene oxide using much less acid. *Mater Today Phys* 9:100097. <https://doi.org/10.1016/J.MTPHYS.2019.100097>
- Melo DQ, Lima ACA, Barros AL, et al (2014) Equilíbrio de adsorção
- Moussout H, Ahlafi H, Aazza M, Maghat H (2018) Critical of linear and nonlinear equations of pseudo-first order and pseudo-second order kinetic models. *Karbala Int J Mod Sci* 4:244–254. <https://doi.org/10.1016/j.kijoms.2018.04.001>
- Oliveira RL, Kerstien J, Schomäcker R, Thomas A (2020) Pd nanoparticles confined in mesoporous N-doped carbon silica supports: a

- synergistic effect between catalyst and support. *Catal Sci Technol* 10:1385–1394. <https://doi.org/10.1039/c9cy01920k>
- Ostrovskii VE (1989) Mechanism of ammonia synthesis over iron catalysts in the equilibrium region. *Theor Exp Chem* 25:193–201. <https://doi.org/10.1007/BF01135010>
- Pei C, Han G, Zhao Y, Zhao H, Liu B, Cheng L, Yang H, Liu S (2016) Superior adsorption performance for triphenylmethane dyes on 3D architectures assembled by ZnO nanosheets as thin as ~1.5 nm. *J Hazard Mater* 318:732–741. <https://doi.org/10.1016/j.jhazmat.2016.07.066>
- Penner D, Lagaly G (2000) Influence of organic and inorganic salts on the coagulation of montmorillonite dispersions. *Clay Clay Miner* 48:246–255. <https://doi.org/10.1346/CCMN.2000.0480211>
- Prediger P, Cheminski T, De Figueiredo T et al (2018) Journal of Environmental Chemical Engineering Graphene oxide nanomaterials for the removal of non-ionic surfactant from water. *J Environ Chem Eng* 6:1536–1545. <https://doi.org/10.1016/j.jece.2018.01.072>
- Przystas W, Zablocka-Godlewska E, Grabinska-Sota E (2012) Biological removal of azo and triphenylmethane dyes and toxicity of process by-products. *Water Air Soil Pollut* 223:1581–1592. <https://doi.org/10.1007/s11270-011-0966-7>
- Rai HS, Bhattacharyya MS, Singh J et al (2005) Removal of dyes from the effluent of textile and dyestuff manufacturing industry: a review of emerging techniques with reference to biological treatment. *Crit Rev Environ Sci Technol* 35:219–238. <https://doi.org/10.1080/10643380590917932>
- Redlich O, Peterson DL (1959) A useful adsorption isotherm. *J Phys Chem* 63:1024. <https://doi.org/10.1021/j150576a611>
- Ren B, Xu Y, Zhang L, Liu Z (2018) Carbon-doped graphitic carbon nitride as environment-benign adsorbent for methylene blue adsorption: kinetics, isotherm and thermodynamics study. *J Taiwan Inst Chem Eng* 88:114–120. <https://doi.org/10.1016/j.jtice.2018.03.041>
- Rodríguez A, Sáez P, Díez E, Gómez JM, García J, Bernabé I (2019) Highly efficient low-cost zeolite for cobalt removal from aqueous solutions: characterization and performance. *Environ Prog Sustain Energy* 38:S352–S365. <https://doi.org/10.1002/ep.13057>
- Roushani M, Mavaei M, Rajabi HR (2015) Graphene quantum dots as novel and green nano-materials for the visible-light-driven photocatalytic degradation of cationic dye. *J Mol Catal A Chem* 409:102–109. <https://doi.org/10.1016/j.molcata.2015.08.011>
- Satilmis B (2020) Amidoxime modified polymers of intrinsic microporosity (PIM-1); a versatile adsorbent for efficient removal of charged dyes; equilibrium, kinetic and thermodynamic studies. *J Polym Environ* 28:995–1009. <https://doi.org/10.1007/s10924-020-01664-4>
- Senthil Kumar P, Ramalingam S, Senthamarai C, Niranjana M, Vijayalakshmi P, Sivanesan S (2010) Adsorption of dye from aqueous solution by cashew nut shell: studies on equilibrium isotherm, kinetics and thermodynamics of interactions. *Desalination* 261:52–60. <https://doi.org/10.1016/j.desal.2010.05.032>
- Shi W, Ren H, Huang X, Li M, Tang Y, Guo F (2020) Low cost red mud modified graphitic carbon nitride for the removal of organic pollutants in wastewater by the synergistic effect of adsorption and photocatalysis. *Sep Purif Technol* 237:116477. <https://doi.org/10.1016/j.seppur.2019.116477>
- Sims RA, Harmer SL, Quinton JS (2019) The role of physisorption and chemisorption in the oscillatory adsorption of organosilanes on aluminium oxide. *Polymers (Basel)* 11. <https://doi.org/10.3390/polym11030410>
- Sing KSW, Everett DH, Haul RAW et al (1985) Reporting physisorption data for gas/solid systems with special reference to the determination of surface area and porosity. *Pure Appl Chem* 57:603–619. <https://doi.org/10.1351/pac198557040603>
- Sumalinog DAG, Capareda SC, de Luna MDG (2018) Evaluation of the effectiveness and mechanisms of acetaminophen and methylene blue dye adsorption on activated biochar derived from municipal solid wastes. *J Environ Manag* 210:255–262. <https://doi.org/10.1016/j.jenvman.2018.01.010>
- Svoboda L, Škuta R, Matějka V, Dvorský R, Matýsek D, Henych J, Mančík P, Praus P (2019) Graphene oxide and graphitic carbon nitride nanocomposites assembled by electrostatic attraction forces: synthesis and characterization. *Mater Chem Phys* 228:228–236. <https://doi.org/10.1016/j.matchemphys.2019.02.077>
- Tian C, Zhao H, Sun H, Xiao K, Keung Wong P (2020) Enhanced adsorption and photocatalytic activities of ultrathin graphitic carbon nitride nanosheets: kinetics and mechanism. *Chem Eng J* 381:122760. <https://doi.org/10.1016/j.cej.2019.122760>
- Vidal CB, Barros AL, Moura CP, de Lima ACA, Dias FS, Vasconcelos LCG, Fachine PBA, Nascimento RF (2011) Adsorption of polycyclic aromatic hydrocarbons from aqueous solutions by modified periodic mesoporous organosilica. *J Colloid Interface Sci* 357:466–473. <https://doi.org/10.1016/j.jcis.2011.02.013>
- Wan S, Ou M, Wang Y, Zeng Y, Xiong Y, Song F, Ding J, Cai W, Zhang S, Zhong Q (2019) Protonic acid-assisted universal synthesis of defect abundant multifunction carbon nitride semiconductor for highly-efficient visible light photocatalytic applications. *Appl Catal B Environ* 258:118011. <https://doi.org/10.1016/J.APCATB.2019.118011>
- Wang L, Zhang J, Zhao R, Li C, Li Y, Zhang C (2010) Adsorption of basic dyes on activated carbon prepared from *Polygonum orientale* Linn: equilibrium, kinetic and thermodynamic studies. *Desalination* 254:68–74. <https://doi.org/10.1016/j.desal.2009.12.012>
- Wang D, Liu L, Jiang X, Yu J, Chen X (2015) Adsorption and removal of malachite green from aqueous solution using magnetic β -cyclodextrin-graphene oxide nanocomposites as adsorbents. *Colloids Surf A Physicochem Eng Asp* 466:166–173. <https://doi.org/10.1016/j.colsurfa.2014.11.021>
- Wang J, Li M, Qian M, Zhou S, Xue A, Zhang L, Zhao Y, Xing W (2018) Simple synthesis of high specific surface carbon nitride for adsorption-enhanced photocatalytic performance. *Nanoscale Res Lett* 13. <https://doi.org/10.1186/s11671-018-2654-7>
- Weber WJ, Morris JC (1963) Kinetics of adsorption on carbon from solution. *J Sanit Eng Div Proc* 89:31–60
- Wu FC, Liu BL, Wu KT, Tseng RL (2010) A new linear form analysis of Redlich-Peterson isotherm equation for the adsorptions of dyes. *Chem Eng J* 162:21–27. <https://doi.org/10.1016/j.cej.2010.03.006>
- Xiao F, Li H, Yan X, Yan L, Zhang X, Wang M, Qian C, Wang Y (2020) Graphitic carbon nitride/graphene oxide (g-C₃N₄/GO) nanocomposites covalently linked with ferrocene containing dendrimer for ultrasensitive detection of pesticide. *Anal Chim Acta* 1103:84–96. <https://doi.org/10.1016/j.aca.2019.12.066>
- Xu C, Qiu P, Chen H, Zhou Y, Jiang F, Xie X (2016) Pd/mesoporous carbon nitride: a bifunctional material with high adsorption capacity and catalytic hydrodebromination activity for removal of tetrabromobisphenol A. *Colloids Surfaces A Physicochem Eng Asp* 506:654–663. <https://doi.org/10.1016/j.colsurfa.2016.07.050>
- Xu C, Wang J, Gao B, Dou M, Chen R (2019) Synergistic adsorption and visible-light catalytic degradation of RhB from recyclable 3D mesoporous graphitic carbon nitride/reduced graphene oxide aerogels. *J Mater Sci* 54:8892–8906. <https://doi.org/10.1007/s10853-019-03531-7>
- Yagub MT, Sen TK, Afroz S, Ang HM (2014) Dye and its removal from aqueous solution by adsorption: a review. *Adv Colloid Interf Sci* 209:172–184. <https://doi.org/10.1016/j.cis.2014.04.002>

- Ye S, Feng J (2016) The effect of sonication treatment of graphene oxide on the mechanical properties of the assembled films. *RSC Adv* 6: 39681–39687. <https://doi.org/10.1039/C6RA03996K>
- Yi F, Ma J, Lin C, Wang L, Zhang H, Qian Y, Zhang K (2020) Insights into the enhanced adsorption/photocatalysis mechanism of a Bi₄O₅Br₂/g-C₃N₄ nanosheet. *J Alloys Compd* 821:153557. <https://doi.org/10.1016/j.jallcom.2019.153557>
- Zhang J, Guo F, Wang X (2013) An optimized and general synthetic strategy for fabrication of polymeric carbon nitride nanoarchitectures. *Adv Funct Mater* 23:3008–3014. <https://doi.org/10.1002/adfm.201203287>
- Zhang S, Wang X, Li J, Wen T (2014a) Efficient removal of a typical dye and Cr(VI) reduction using N-doped magnetic porous carbon †. *RSC Adv* 4:63110–63117. <https://doi.org/10.1039/c4ra10189h>
- Zhang W, Huang H, Li F, Deng K, Wang X (2014b) Palladium nanoparticles supported on graphitic carbon nitride-modified reduced graphene oxide as highly efficient catalysts for formic acid and methanol electrooxidation. *J Mater Chem A* 2:19084–19094. <https://doi.org/10.1039/c4ta03326d>
- Zhao C, Fan J, Chen D, Xu Y, Wang T (2016) Microfluidics-generated graphene oxide microspheres and their application to removal of perfluorooctane sulfonate from polluted water. *Nano Res* 9:866–875. <https://doi.org/10.1007/s12274-015-0968-7>

Publisher's note Springer Nature remains neutral with regard to jurisdictional claims in published maps and institutional affiliations.